Acta Materialia 243 (2023) 118514

Contents lists available at ScienceDirect

Acta Materialia

journal homepage: www.elsevier.com/locate/actamat

Full length article

Global understanding of deformation behavior in CoCrFeMnNi high entropy alloy under high-strain torsion deformation at a wide range of elevated temperatures

Reza Gholizadeh[a,*], Shuhei Yoshida[a], Yu Bai[a,b,c], Shu Kurokawa[a], Akinobu Shibata[a,b,d], Nobuhiro Tsuji[a,b,*]

[a] Department of Materials Science and Engineering, Kyoto University, Sakyo-ku, Kyoto 606-8501, Japan
[b] Elements Strategy Initiative for Structural Materials (ESISM), Kyoto University, Sakyo-ku, Kyoto 606-8501, Japan
[c] School of Materials Science and Engineering, Dalian University of Technology, Dalian 116024, China
[d] Research Center for Structural Materials, National Institute for Materials Science (NIMS), 1-2-1 Sengen, Tsukuba 305-0047, Japan

ARTICLE INFO

Article history:
Received 22 April 2022
Revised 6 November 2022
Accepted 11 November 2022
Available online 12 November 2022

Keywords:
High entropy alloy
Deformation microstructure
Deformation twinning
Intermediate-temperature embrittlement
Dynamic recrystallization

ABSTRACT

A number of recent studies have investigated deformation behavior of CoCrFeMnNi (Cantor) alloy at elevated temperatures by using plastic deformation to relatively small strains such as tensile testing. Therefore, little has been known about the deformation behavior of this typical FCC high-entropy alloy (HEA) in case that the material is subjected to ultra-high strains at various temperatures. In the present study, the equi-atomic CoCrFeMnNi HEA was successfully deformed over a wide range of strains (von Mises equivalent strains (ε) of 1∼5.5) by torsion at various temperatures ranging from 25 °C to 1100 °C. Deformation twinning was extensively activated at moderate to high strains ($\varepsilon \geq 1$) and even found in the deformation at elevated temperatures as high as 600 °C where deformation twinning is not normally expected in Cantor alloy. The HEA showed outstanding deformability and the highest strains to fracture reached 4.0∼5.5 at low temperatures below 400 °C. The excellent deformability was attributed to the extensive twin activities including the formation of twin bundles and thin nanotwins as well as microbands formation. However, localized shear deformation that was promoted by the high straining at low temperatures could negatively affect the deformability. The heavy deformation led to a significant reduction of the grain sizes down to 50 nm∼150 nm. A sudden shortage of ductility occurred at intermediate temperatures, where small strains to fracture (1.2∼1.3) were realized at 600 °C∼700 °C. The embrittlement was accompanied by the formation of micro-voids at grain boundaries and intergranular fracture. The susceptibility to the embrittlement was caused by the precipitation of Cr-rich σ-phases at grain boundaries. Dynamic recrystallization (DRX) of the FCC matrix led to an accelerated softening at high temperatures above 600 °C. Nucleation and growth of DRX grains in Cantor alloy were not fundamentally different from those in conventional FCC alloys. This study gives an insight into the microstructure evolution and mechanical response in Cantor alloy under shear deformation over a wide range of strains and temperatures.

1. Introduction

Unlike conventional alloys that have one or two major elements, the novel high-entropy alloys (HEAs) are composed of at least five principal elements, with concentrations of 5 at% to 35 at% for each component [1]. As initially proposed by Yeh et al. [1], high mixing entropy plays a significant role for stabilizing solid solutions in high-concentration multi-element systems. Cantor et al. [2] developed an equi-atomic CoCrFeMnNi high-entropy alloy having a single FCC (face centered cubic) solid solution that has been called Cantor alloy. Cantor alloy has become one of the most studied FCC HEAs in the field by now. Superior mechanical properties of Cantor alloy make it a potential candidate for low- and high-temperature applications [3,4].

Deformation mechanisms in the CoCrFeMnNi HEA have been studied mainly by employing uniaxial tensile tests at different tem-

* Corresponding authors.
E-mail addresses: gholizadeh.reza.8a@kyoto-u.ac.jp (R. Gholizadeh), nobuhiro-tsuji@mtl.kyoto-u.ac.jp (N. Tsuji).

https://doi.org/10.1016/j.actamat.2022.118514

peratures [5–11]. Tensile deformation at cryogenic temperatures promotes mechanical twinning in the FCC matrix of the HEA having low stacking fault energy (SFE: 20∼30 mJ/m^2 [12–14]). Twin boundaries can act as obstacles to dislocation movements, and thus they reduce the dislocation mean slip length. This so-called dynamic Hall-Petch effect provides high strain-hardening leading to high strength and large ductility of the HEA at cryogenic conditions [5–7,11]. In tensile deformation at ambient temperature, however, both strength and ductility decrease due to the insufficient twinning activity. It has been considered that the flow stress at ambient temperature does not reach the stress required for the onset of twinning until a late stage of the tensile test close to the macroscopic necking of tensile specimen, as has been stated in recent articles [11,15,16]. In tensile tests at elevated temperature, formations of dislocation tangles and cell structures are promoted. Thermal softening caused by dynamic restoration phenomena makes a great impact on the flow behavior of the HEA at high temperatures [5–11].

Tensile tests can give relatively small-scale plastic deformation (logarithmic true strain $<$ 1.0), because the plastic instability (macroscopic necking) soon leads to the specimen fracture. A few studies on high-pressure torsion (HPT) of the CoCrFeMnNi HEA have been conducted [17–19]. Those studies reported large fractions of deformation twins formed in the HEA during HPT deformation at ambient temperature. It is expected that large plastic strains applied by HPT raise the internal stress to a level that can activate deformation twinning at ambient temperature and potentially at elevated temperatures. Overall, little is known about deformation behavior of the CoCrFeMnNi HEA subjected to high strains at elevated temperatures, even though it is important to know such deformation behavior for considering fabrication processing, like thermo-mechanically controlled processing (TMCP) at various temperatures, of Cantor alloy and its family.

The present study aims to give an insight into the plasticity and deformation microstructures of the CoCrFeMnNi HEA over wide ranges of strains and temperatures. Torsion deformation was used for the purpose in this study. Torsion testing has been commonly used to simulate conventional metal-working processes such as multi-pass rolling and forging. Very large plastic strains can be applied by torsion before fracture occurs. We systematically discuss the correlation between deformation microstructures and mechanical responses in the HEA subjected to the high-strain torsion deformation at different temperatures.

2. Experimental methods

A near equi-atomic CoCrFeMnNi HEA with a chemical composition of 19.90 Co, 20.01 Cr, 20.09 Fe, 19.94 Mn, and 20.07 Ni (in at%) was used in this study. The HEA was fabricated by vacuum induction melting and then cast into an ingot 75 mm in diameter and 140 mm in height. The cast ingot was then hot forged at 1150 °C into a plate with a thickness of 15 mm. The purpose of hot forging was to break down the as-cast (dendritic) microstructure and homogenize the chemical composition in the material. The hot-forged plate was machined into torsion specimens having a gage part of 6 mm in diameter and 3 mm in length (more details in supplementary information, **Fig. S1**). A thermo-mechanical processing simulator (Thermecmastor-TS; Fuji-Dempa Electronics, Co. Ltd.) was used for torsion deformation. Torsion tests were conducted in a temperature range from 25 °C to 1100 °C under an inert gas (Argon) atmosphere to prevent specimens from oxidation. Specimens were heated to test temperatures with a rate of 5 °C s^{-1} by induction heating system and held for three minutes before torsion deformation for homogenizing the temperature of the gage part. Temperatures of the specimen were monitored by thermo-couple for controlling a constant temperature in the gage part during the deformation. Immediately after the end of the deformation, a water-jet system quenched the specimens. In a few cases for preserving fractured surfaces of the specimens, nitrogen-gas cooling was used instead of water cooling. Torsion torque was continuously measured during the deformation. Shear strain and shear stress in torsion were determined according to Fields-Backofen analysis [20], and then shear values were converted to equivalent strain and equivalent stress using von-Mises criterion.

Microstructural characterizations were conducted by employing scanning electron microscopy (SEM), scanning transmission electron microscopy (STEM), atom probe tomography (APT), and X-ray diffraction (XRD). Electron backscattering diffraction (EBSD) measurements and energy dispersive X-ray spectroscopy (EDS) were conducted in a field emission scanning electron microscope, FE-SEM (JEOL-JSM 7100F). EBSD data were processed by the EDAX-TSL OIM software. Electron channeling contrast imaging (ECCI) and fracture surface analysis were conducted in a FE-SEM (JEOL-JSM 7800F). Conventional TEM observations were performed in a JEOL-JEM 2010 TEM operated at 200 kV. High-angle annular dark field (HAADF) imaging and EDS analysis in scanning TEM (STEM-EDS) mode were performed in a JEOL-JEM 2100F. Needle-shape APT samples were fabricated from initial grain boundaries in the deformed specimens by using a site-specific lift-out method in a FEI Quanta 3D 200i dual-beam instrument equipped with focused-ion beam (FIB) milling. APT experiments were conducted in a Cameca Local Electrode Atom Probe (LEAP) 4000XHR instrument using a laser mode with laser pulse energy of 110 pJ, pulse rate of 200 kHz, detection rate of 0.5%, and stage temperature of 50 K. Three-dimensional reconstruction of obtained data sets was performed using Integrated Visualization and Analysis Software (IVAS) 3.8.10. Phase identifications by XRD were carried out in a PANalytical X'Pert PRO Alpha-1 system using Cu Kα radiation. Microstructure characterizations were conducted on sections normal to the radial direction (RD) of the torsion specimens at a radial distance of 0.9 $\times$ R (the radius of the torsion specimen, 3 mm) from the center (300 μm below the surface). For SEM experiments, the sections were prepared by standard mechanical polishing procedures and final polishing with a 0.04 μm colloidal silica suspension. TEM thin foils were prepared by twin-jet electropolishing using a 10%$HClO_4$ + 90%CH_3COOH solution.

3. Results and discussion

3.1. Initial microstructure

Figure 1 shows starting conditions of the equi-atomic CoCrFeMnNi HEA before torsion deformation. Figure 1a displays an EBSD boundary map with red, blue, and green lines representing annealing twin boundaries (Σ3-type), high angle boundaries (misorientation $\theta \geq 15°$), and low angle boundaries ($2° \leq \theta < 15°$), respectively. The starting microstructure was uniformly composed of equiaxed grains surrounded by high angle boundaries. A high fraction of annealing twins could also be realized. The average grain size including twin boundaries (TBs) was around 16 μm. Figure 1b shows the result of phase identification by XRD, indicating that the HEA had a single-phase FCC structure. Additionally, elemental distributions in the starting microstructure were determined by SEM-EDS. The result of EDS analysis along the white arrow marked in the SEM image (Fig. 1c) is represented in Fig. 1d. Distributions of all the five major elements were close to the nominal equi-atomic composition of 20 at% ($\pm$ 2 at%).

3.2. Stress-strain curves

Figure 2 shows the (von Mises) equivalent stress (σ_{eq}) - equivalent strain (ε_{eq}) curves in torsion deformation of the CoCr-

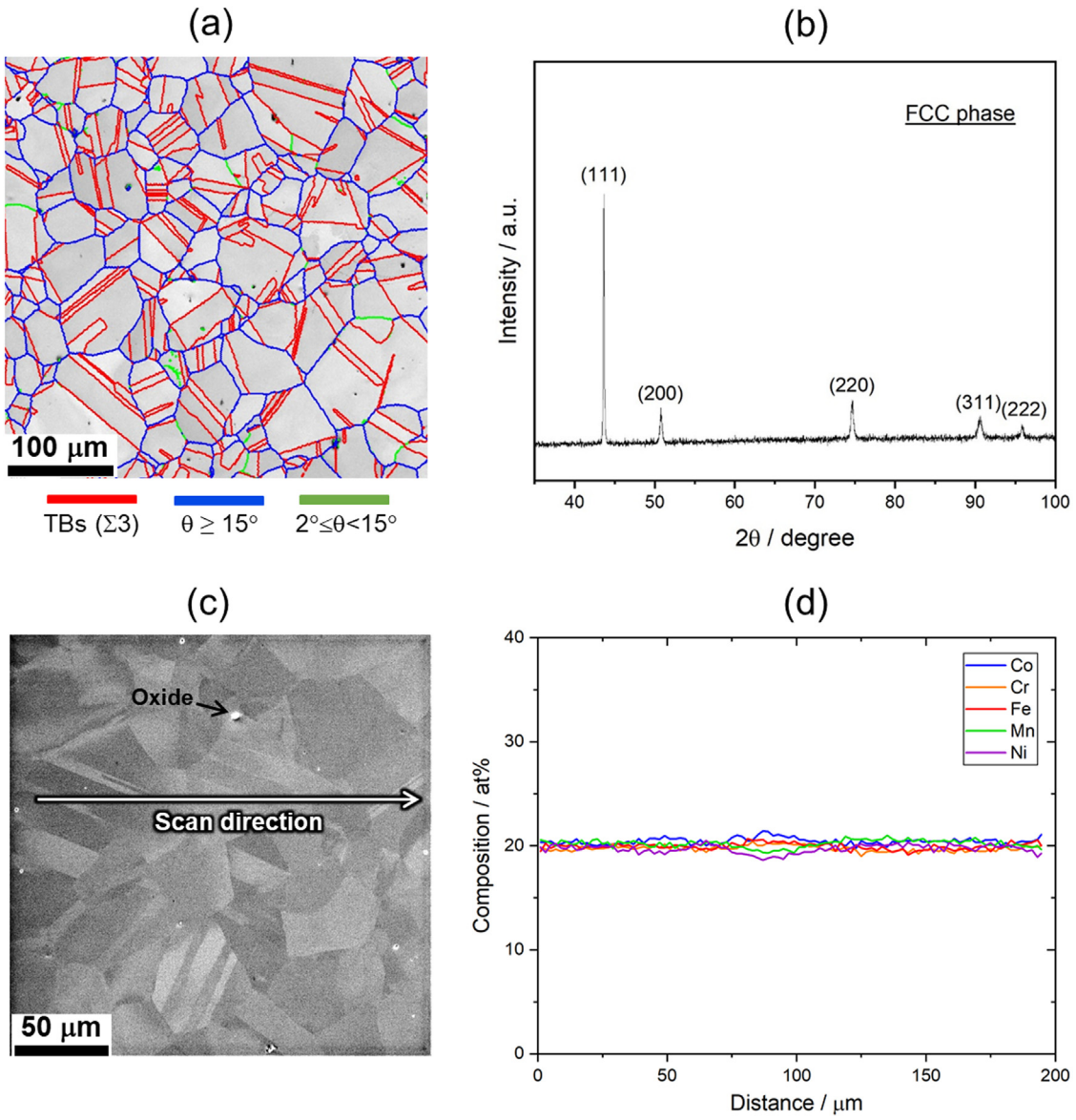

Fig. 1. Initial conditions before the torsion tests of the equi-atomic CoCrFeMnNi HEA used in the present study. (a) EBSD boundary maps overlaid on image quality map. Red, blue, and green lines indicate annealing twin boundaries (Σ3), high angle boundaries ($\theta \geq 15°$), and low angle boundaries ($2° \leq \theta < 15°$), respectively. (b) Phase analysis by XRD. (c) SEM image in which a white arrow indicates the scanning direction for the EDS analysis, of which the result is shown in (d).

FeMnNi HEA. Hereafter, to make the description simple, the terms "stress" and "strain" are used instead of "equivalent stress" and "equivalent strain" in torsion, except in some parts that clarification is required. Torsion tests were conducted at various temperatures ranging from 25 °C to 1100 °C, using different strain rates of 0.01 s^{-1} (Fig. 2a) and 0.1 s^{-1} (Fig. 2b). Almost all specimens were deformed till fracture occurred. Circle markers are used to show the fracture points on the flow stress curves, where the noticeable stress drops are found due to the formation of first cracks in the specimens. Some test temperatures (25 °C, 100 °C) are marked by asterisks (*), denoting that a temperature generated by the plastic deformation was detected during the tests (Supplementary **Fig. S2a**). As can be seen in Fig. 2, strength of the HEA decreased monotonously with increasing the deformation temperature. At a constant temperature, the flow stress was higher at the higher strain rate although such strain-rate sensitivity was noticeable only at temperatures above 600 °C. There was a clear difference in the flow behavior between low and high temperatures. The flow stress at temperatures below 600 °C showed a rapid increase at early stages of deformation, followed by a strain-hardening stage till fracture. The flow stress above 600 °C displayed a maximum stress, followed by a softening stage towards the fracture. It was noteworthy that the HEA was less deformable in a range of intermediate temperatures. Small equivalent strains to the fracture (ε_f: 1.2∼1.3) were realized in the torsion deformation at temperatures of 600 °C and 700 °C.

Figure 3 summarizes the temperature-dependence of mechanical properties of the CoCrFeMnNi HEA. The strength and fracture strain determined by the torsion tests in the current study are plotted as a function of the deformation temperature in Fig. 3a and 3c, respectively. The strength and fracture strain are defined as the (von Mises) equivalent stress and equivalent strain measured at the fracture point in torsion. For comparison, mechanical properties reported in tensile studies of the CoCrFeMnNi HEA are represented in Fig. 3b, 3d [6,9,10,21]. For the tensile tests, the strength is the ultimate tensile strength, and the fracture strain is the total elongation to fracture. As shown in Fig. 3a, the material strength in torsion decreased slowly with increasing temperature up to 600

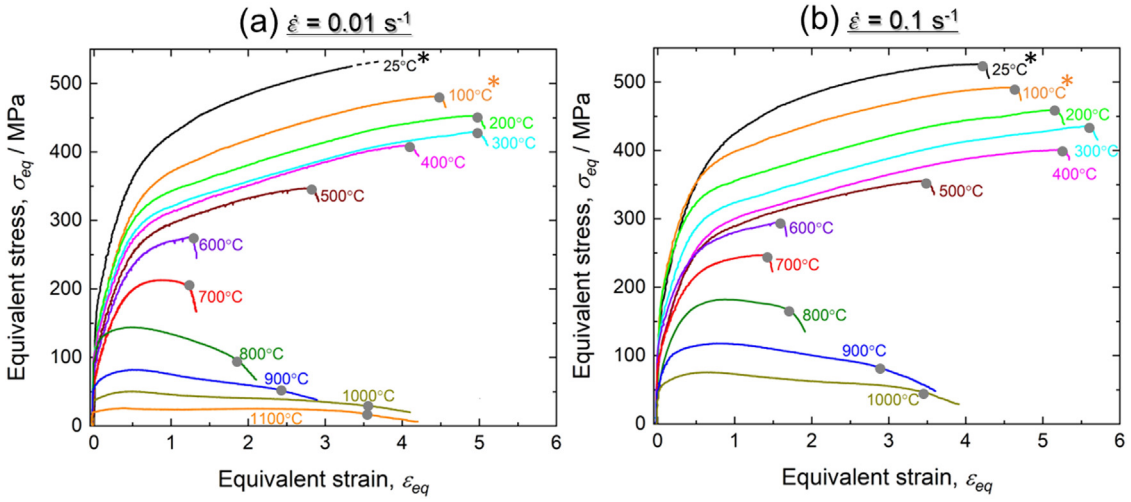

Fig. 2. Equivalent stress (σ_{eq}) - equivalent strain (ε_{eq}) curves in torsion deformation of the CoCrFeMnNi HEA. The torsion tests were carried out at various temperatures from 25 °C to 1100 °C using strain rates of (a) 0.01 s^{-1} and (b) 0.1 s^{-1}. Gray circles on the flow stress curves marked the fracture points under different deformation conditions. Note that temperature rising caused by the plastic deformation was detected during the tests at low temperatures (marked by asterisks: 25 °C*, 100 °C*). In (a), the test at 25 °C could not be completed up to the fracture point. The long duration of the test at the strain rate of 0.01 s^{-1} together with the high load required for the deformation at room temperature was out of the capacity of the torsion machine.

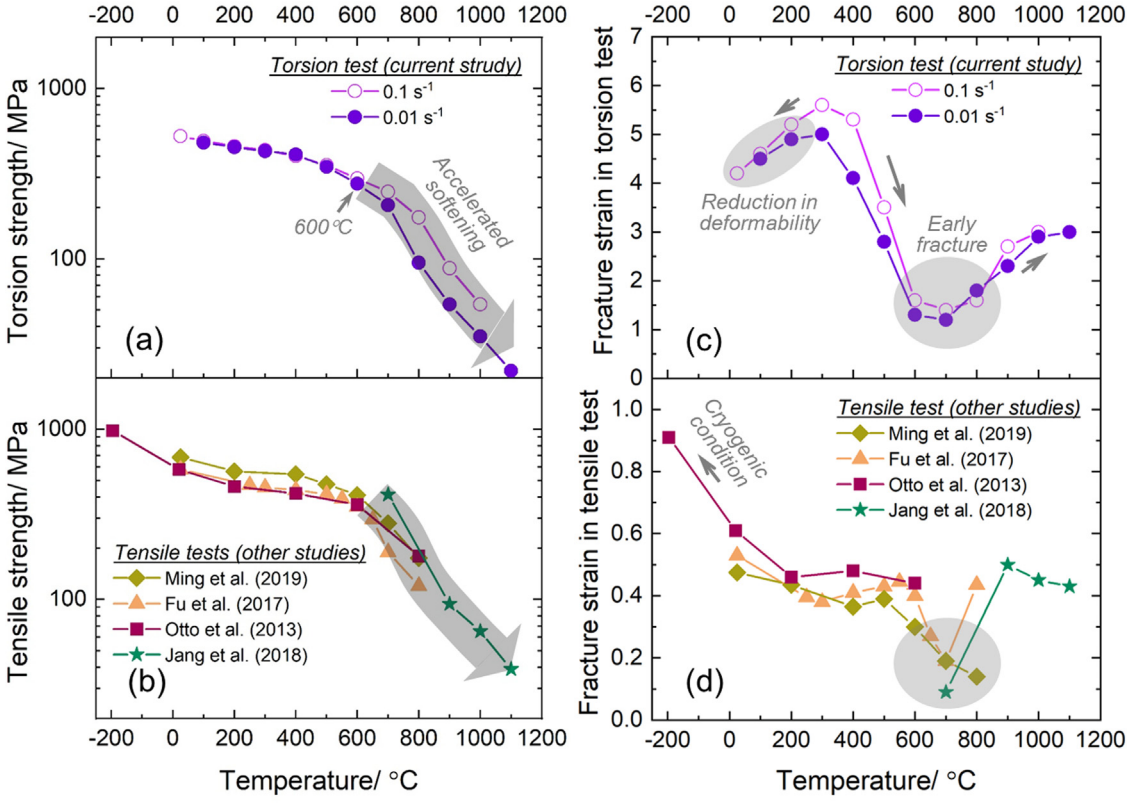

Fig. 3. Temperature-dependence of mechanical properties in the equi-atomic CoCrFeMnNi HEA. (a, b) Strength and (c, d) fracture strain plotted as a function of temperature. Data determined by the torsion test in the current study are shown in (a) and (c). For comparison, data obtained by tensile tests in other studies [6,9,10,21] are summarized in (b) and (d). Here the torsion strength in (a) is the von Mises equivalent flow stress at the fracture strain (fracture points are marked on the flow stress curves shown in Fig. 2). For the tensile tests, strength is the ultimate tensile strength, and fracture strain is the total elongation to fracture [6,9,10,21]. All tensile tests were conducted at nearly the same strain rate ~ 10^{-3} s^{-1}.

°C, and then it quickly dropped at higher temperatures. The tensile strength reported in the literature exhibits the same tendency with increasing deformation temperature (Fig. 3b). The effect of temperature on the fracture strain was somewhat complicated. As represented in Fig. 3c, the HEA showed high fracture strains of 4.0~5.5 at low temperatures, at least up to ~400 °C. Note that the material's deformability slightly reduced in the temperature range from 300 °C to room temperature under the high-strain torsion. In this respect, the tensile results show an opposite tendency since the tensile ductility increases with decreasing temperature, especially at cryogenic temperatures (Fig. 3d). The fracture strain in Fig. 3c dramatically dropped at intermediate temperatures of 600 °C~800

C°, and it increased again at high temperatures above 800 °C. The ductility loss at intermediate temperatures has also been realized in former tensile results of the CoCrFeMnNi HEA reported in other studies (Fig. 3d). A similar phenomenon can be found in equi-atomic ternary and quaternary alloys such as CoCrNi and CoCrFeNi [22]. In general, the susceptibility of conventional metallic materials to intermediate-temperature embrittlement is mainly related to the elemental segregation at grain boundaries [23–25]. The underlying mechanism to the embrittlement in the current CoCrFeMnNi is discussed in section 3.4.

3.3. Deformation microstructures at $T \leq 600$ °C

For a smooth discussion, we simply consider that 600 °C is a transition temperature between the low-temperature and high-temperature deformations in the HEA, according to the change of the strength shown in Fig. 3a. The assessment was based on the fact that a rapid thermal softening at temperatures above 600 °C was realized in the HEA (Fig. 3a). Deformation microstructures at some representative low temperatures (100 °C, 400 °C, and 600 °C) are discussed in this section and those at high temperatures (> 600 °C) are discussed separately in a later section 3.5.

3.3.1. Microstructure evolution at 100 °C

The HEA was deformed to different equivalent strains at 100 °C ($\dot{\varepsilon} = 0.01\ s^{-1}$). Figure 4**a-f** show representative deformation microstructures at $\varepsilon = 1.0$. Microstructures were observed from the radial direction RD, i.e., on the section containing the shear plane normal SPN and the shear direction SD. The IPF (inverse pole figure) map in Fig. 4a shows that initial grains were deformed and highly elongated towards SD. Deformed grains contained noticeable fractions of deformation twins (Ts) with characteristic $\Sigma 3$-boundaries indicated by red lines in the EBSD boundary map (Fig. 4b). It seemed that twins were preferably aligned along SD. Intense localized deformation in the form of shear bands (SBs) could be found in some grains locally (Fig. 4a). Bright-field (BF) TEM images in Fig. 4c-**f** demonstrate details of substructures in the deformed matrix. The substructures greatly varied from one grain to another grain. Selected area diffraction (SAD) patterns (Fig. 4 **c1, d1, d2, e1, f1**) were obtained along [011] zone axis to characterize substructures in the observed regions. Deformation twins predominantly existed in almost all grains. They mostly formed as twin bundles with an average total width of ~1 μm (Fig. 4c). Twins seemed to emit from initial grain boundaries (GBs). There were steps on the GBs from which the twin bundles initiated or terminated. The SAD pattern shown in Fig. 4c1 corresponds to a twin bundle located inside the rectangular region displayed in Fig. 4c. A diffraction spot encircled in Fig. 4c1 was used to obtain a dark-field image of the twin bundle (Fig. 4c2)**.** The bundle was composed of several finely-spaced nanotwins. The width of individual nanotwins was in a range of ten to hundred nanometers. Figure 4d shows a shear band that penetrated early-formed twin-matrix (TM) lamellae. Twin boundaries adjacent to the SB were bended. The substructure inside the SB had elongated shapes along the direction of SB propagation. The comparison of SAD patterns associated to the neighboring TM lamellae (Fig. 4d1) and the SB (Fig. 4d2) indicates that the matrix inside the SB was re-oriented ~20° around [011] crystallographic axis. At the moderate strain of 1, the shear banding behavior was observed in a fraction of grains. By further straining from the moderate strain to high strains (>1), the phenomenon was intensified (Supplementary **Fig. S2b-d**) as dislocation slip and twinning in the strain-hardened matrix became difficult [26]. The localized shear deformation could also cause a local temperature rise inside the SB. Accordingly, an increase in the overall temperature of torsion specimens could happen although the magnitude of the temperature rise was not significant under the quasi-static torsion deformation (Suppl. **Fig. S2a**). Microbands (MBs) [26–29] could be also found in the specimen strained to $\varepsilon = 1.0$ at 100 °C (Fig. 4e). Nanotwins were observed in some regions with former banded structures (Fig. 4f).

Figure 4g and 4h are BF-TEM images in the specimen deformed up to the fracture strain of 4.5. The high-strain deformation resulted in the formation of a lamellar nanostructure (Fig. 4g). The average width of lamellae (d) was around 50 nm. The formation of the nanostructured lamellae could be explained by the grain subdivision mechanism [19,27–30]. That is, deformation-induced boundaries such as twin boundaries and geometrically necessary boundaries (e.g., MBs) subdivide the deformed matrix. The number of deformation-induced boundaries increases with increasing the plastic strain. Thus, the average boundary spacing continuously decreases, leading to extensive grain refinement at high strains. It should be mentioned that the deformation twins that formed at early stage of deformation gradually lose their boundary coherency. The twin boundaries become normal high-angle boundaries during the refinement process since they crystallographically rotate by plastic deformation and interact with dislocations and other microstructural features such as SBs and MBs [19]. It is expected that the formation of new twins is suppressed with the grain refinement [16]. However, twins could still form within the nanosized lamellae of the HEA, as shown in Fig. 4h. The result indicated that extensive twin activity occurred over a wide range of strains at 100 °C.

3.3.2. Microstructure evolution at 400 °C

Figure 5**a-d** show representative microstructures developed in the specimen strained to $\varepsilon = 1.0$ at 400 °C ($\dot{\varepsilon} = 0.01\ s^{-1}$). EBSD maps shown in Fig. 5a and 5b did not reveal any twin formation in the deformed matrix, in contrast to the EBSD microstructure deformed at 100 °C (Fig. 4a, 4b). Twinning mechanism was clearly suppressed with increasing temperature. Twinning activity was, however, not completely prevented at 400 °C. The BF-TEM image shown in Fig. 5c and corresponding SAD pattern (Fig. 5c1) revealed that substructures contained a fraction of deformation twins. The nanotwins had average thicknesses smaller than 100 nm. Thus, they were difficult to be characterized in the EBSD analysis (Fig. 5a, 5b) unless the step size in the EBSD scanning was below 100 nm. The suppression of twinning is mostly attributed to the fact that the flow stress at elevated temperatures does not reach high levels to activate the twinning mechanism [11,15,16]. In the absence of strong twinning activities, microband formation became the dominant microstructural feature at 400 °C, as shown in Fig. 5d. Figure 5e is a BF-TEM image of a nanostructured HEA that was observed at the fracture strain of 4.1 at 400 °C. The nanostructure had quasi-lamellar morphologies with an average boundary spacing of d~150 nm. The corrugated lamellar boundaries indicated that short-range boundary migration was (thermally) activated at 400 °C.

3.3.3. Microstructure evolution at 600 °C

Figure 6 represents deformation microstructures in the specimen deformed to $\varepsilon = 1.0$ at 600 °C ($\dot{\varepsilon} = 0.01\ s^{-1}$). Note that further straining of the HEA at 600 °C was not possible since the specimen soon fractured at a strain of ~1.3. No deformation twins were recognized, at least in the EBSD measurements with the step size of 0.1 μm (Fig. 6a, 6b). Nonetheless, the TEM observation revealed a small number of thin nanotwins that were sporadically distributed within the deformed matrix (Fig. 6c). The thickness of nanotwins was smaller than 20 nm. The deformed matrix was mainly subdivided by microbands (Fig. 6d). In this respect, the microstructure evolution at 600 °C was comparable to that found at 400 °C (Fig. 5c, 5d). As pointed out in the ECC image shown in

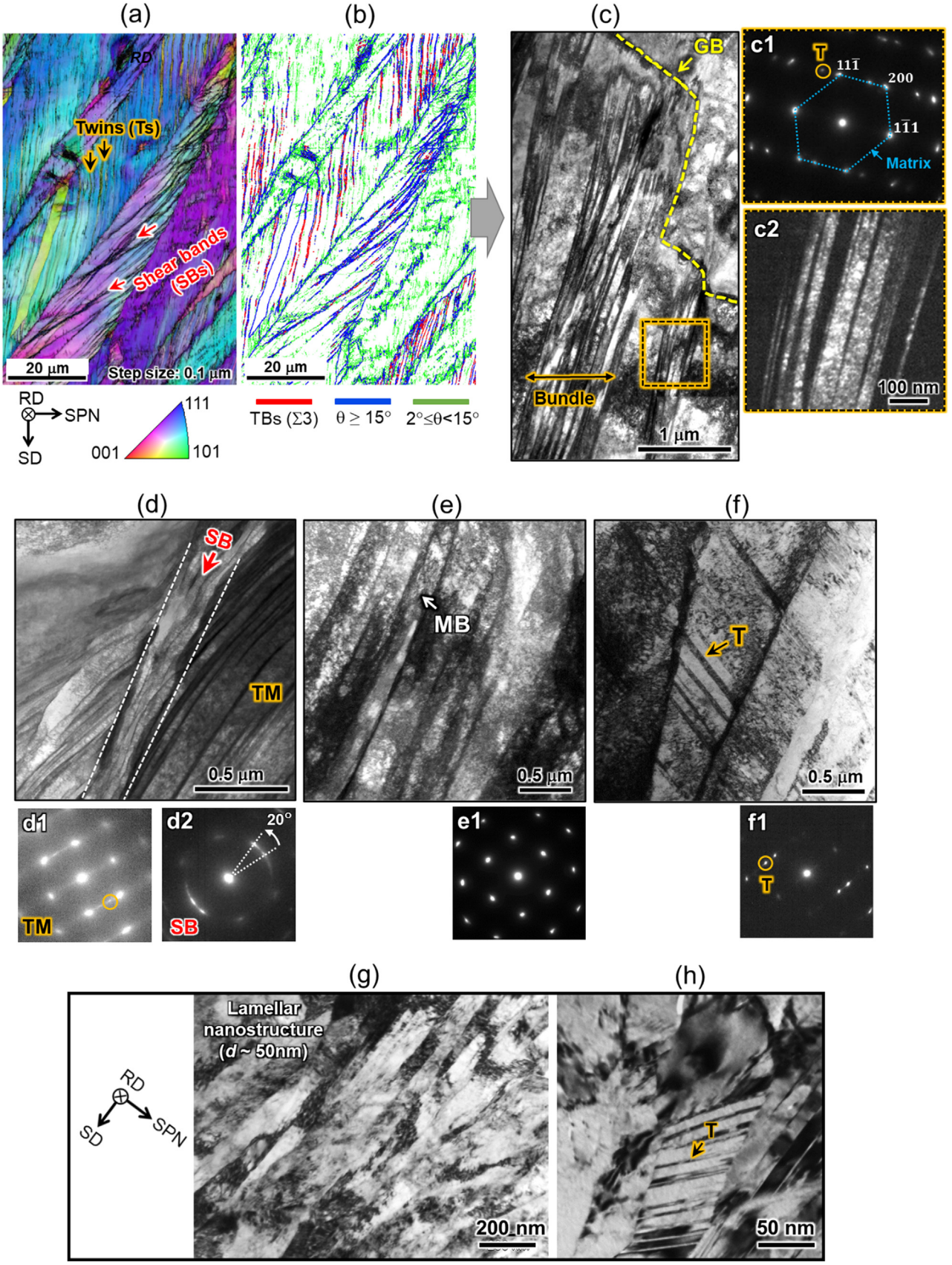

Fig. 4. Microstructure evolution in the CoCrFeMnNi HEA deformed to different equivalent strains at 100 °C and 0.01 s^{-1}. (a) EBSD-IPF (inverse pole figure) map overlaid on IQ (image quality) map, (b) EBSD boundary map, (c-f) bright-field TEM images and corresponding SAD patterns (c1, d1, d2, e1, f1) obtained along [011] zone axis, all in the specimen deformed to $\varepsilon = 1.0$. Red, blue, and green lines in (b) indicate twin boundaries ($\Sigma 3$), high angle boundaries ($\theta \geq 15°$), and low angle boundaries ($2° \leq \theta < 15°$), respectively. A dark-field image shown in (c2) corresponds to the rectangular region displayed in (c). The diffraction spot used to obtain the dark-field image is encircled in the SAD pattern shown in (c1). (g-h) Bright-field TEM images in the specimen highly-deformed to the fracture strain (ε_f) of 4.5. All microstructures were viewed from the radial direction (RD) normal to the SPN-SD plane. SPN and SD are the shear plane normal and shear direction in torsion, respectively.

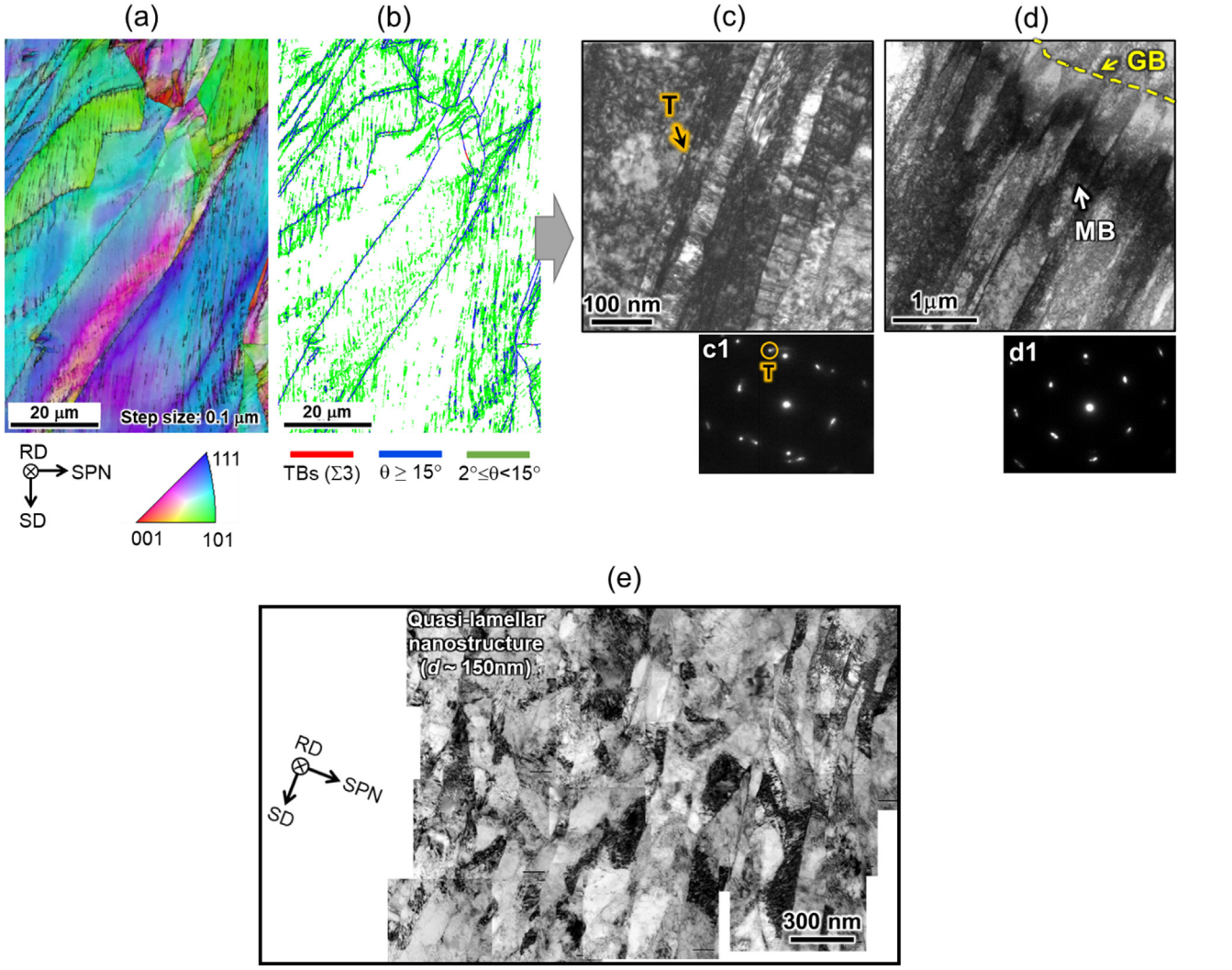

Fig. 5. Microstructure evolution in the CoCrFeMnNi HEA deformed to different equivalent strains at 400 °C and 0.01 s^{-1}. (a) EBSD-IPF map overlaid on IQ map, (b) EBSD boundary map, (c-d) bright-field TEM images and corresponding SAD patterns (c1, d1) obtained along [011] zone axis, all in the specimen deformed to $\varepsilon = 1.0$. Red, blue, and green lines in (b) indicate twin boundaries (Σ3), high angle boundaries ($\theta \geq 15°$), and low angle boundaries ($2° \leq \theta < 15°$), respectively. (e) Bright-field TEM image in the specimen highly-deformed to the fracture strain (ε_f) of 4.1. All microstructures were viewed from the radial direction (RD) normal to the SPN-SD plane.

Fig. 6e, micro-voids were frequently found at this stage of the deformation just before fracture. The micro-voids were aligned on one line (probably an initial grain boundary). The enlarged ECC image in Fig. 6f is taken from a GB region where the micro-voids were decorated along the GB. It is considered that the early failure of the specimen deformed at 600 °C was related to the formation and coalescence of the micro-voids at the GBs, which will be discussed in the later section 3.4.

According to the microstructure evolution shown through Figs. 4 to 6, the tendency for deformation twinning changes dramatically with the deformation temperature. In general, the transition of deformation mechanism from dislocation slip to deformation twinning is dependent on deformation variables such as temperature and strain rate [31], which can be unifiedly expressed by the Zener-Hollomon (Z) parameter, i.e., $Z = \dot{\varepsilon}\exp(Q/RT)$, where R is the gas constant and Q is the activation energy for deformation [32]. With decreasing the Z parameter, i.e. increasing temperature or decreasing strain rate, the flow stress of plastic deformation decreases and the twinning activity becomes suppressed accordingly [7,11,15,31,33,34]. In other words, lower-Z conditions require higher plastic strains to reach the critical stress for twinning [11]. Thurston et al. [15] reported that the onset of twinning in Cantor alloy happened at (true) strains of ~0.08 at -196 °C, ~0.16 at -75 °C, and ~0.25 at 20 °C under the quasi-static tensile loading. At an elevated temperature of 100 °C under the quasi-static torsion deformation (in the current study), twinning was further delayed until an equivalent strain of ~0.5. The related microstructure is not shown in the paper to save space (see Suppl. **Fig. S4**). Under the torsion deformation at 400~600 °C, twinning was activated at a higher equivalent strain of ~1, although determining the exact strain for the onset of twinning requires further investigation. Based on the Z parameter, decreasing strain rate is expected to have the same impact as increasing temperature on the twinning behavior. Despite, there is not sufficient experimental data in literature on the effect of strain rate on the twinning behavior in Cantor alloy, particularly under the quasi-static loading condition. The current study showed no obvious change in the twinning behavior perhaps due to a weak sensitivity of twinning to a small change in strain rate used in the current study (10^{-2}~10^{-1} s^{-1}). However, a dramatic increase in the strain rate from the quasi-static to dynamic loading conditions promotes the twinning in Cantor alloy [33,34]. For example, Yang et al. [34] studied deformation of Cantor alloy via shear testing of a hat-shape specimen at various strain rates. They reported that the dislocation slip was the dom-

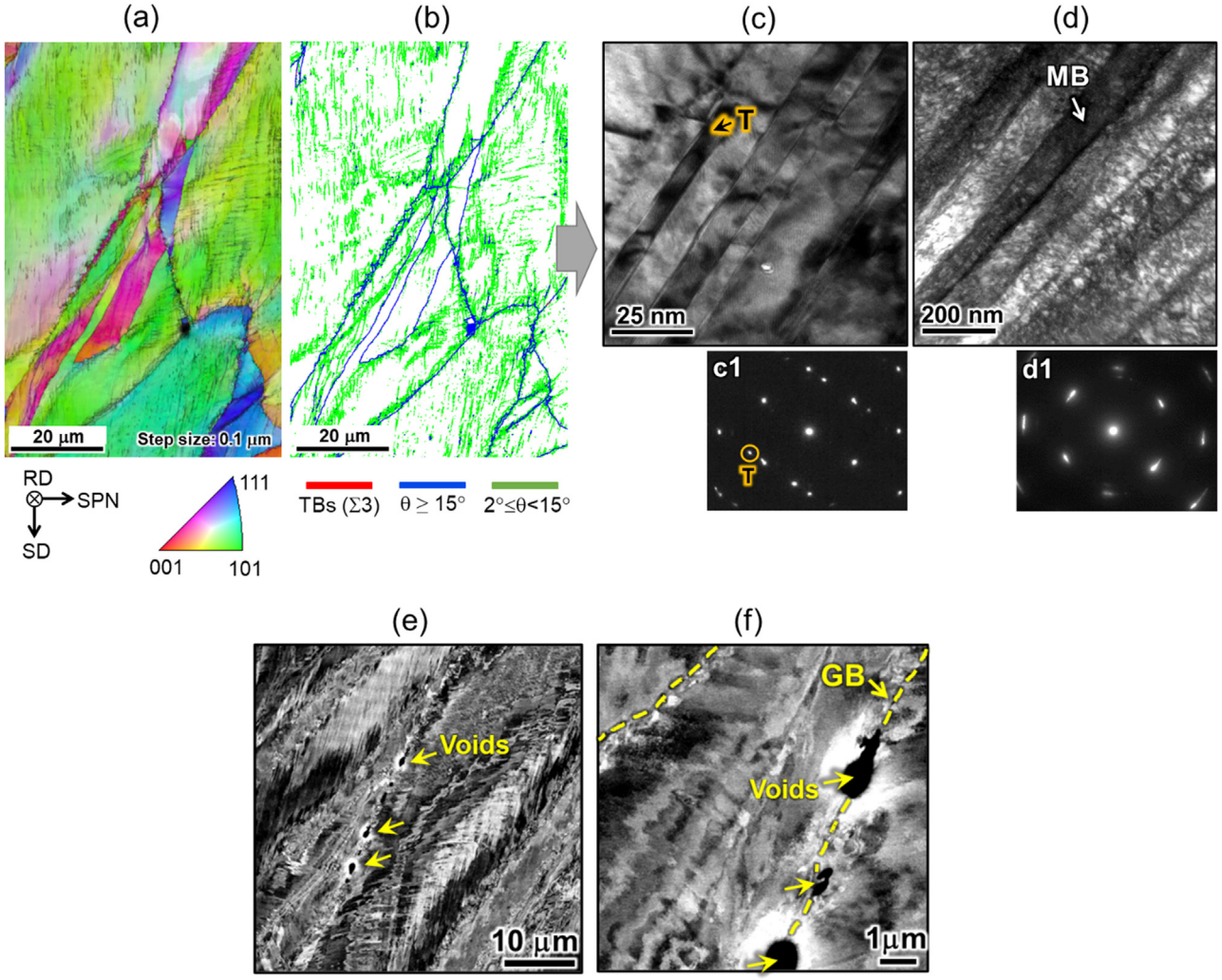

Fig. 6. Microstructure evolution in the CoCrFeMnNi HEA deformed to ε =1.0 at 600 °C and 0.01 s^{-1}. (a) EBSD-IPF map overlaid on IQ map, (b) EBSD boundary map, (c-d) bright-field TEM images and corresponding SAD patterns (c1, d1) obtained along [011] zone axis, (e-f) ECC images. Red, blue, and green lines in (b) indicate twin boundaries (Σ3), high angle boundaries ($\theta \geq 15°$), and low angle boundaries ($2° \leq \theta < 15°$), respectively. All microstructures were viewed from the radial direction (RD) normal to the SPN-SD plane.

inant mechanism up to a shear strain of ~3.4 at a strain-rate of 2×10^{-3} s^{-1}. In contrast, multiple deformation twins were observed in the microstructure deformed to the same shear strain at a strain rate of 5×10^{4} s^{-1}. In addition to the deformation parameters, microstructure variables such as grain size can cause a significant transition of twinning behavior. Sun et al. [16] reported that twinning became suppressed with decreasing the grain size in Cantor alloy, owing to an increase in the critical stress for twinning with the grain refinement.

3.3.4. Strain-hardening behavior at T ≤ 600 °C

Strain-hardening responses of the HEA were analyzed at temperatures of 25 °C to 600 °C. The strain-hardening rates ($\partial\sigma/\partial\varepsilon$), derived from the equivalent stress-strain curves in torsion (Fig. 2), are plotted as a function of equivalent strain in Fig. 7. Figure 7a and 7b correspond to the deformation at strain rates of 0.01 s^{-1} and 0.1 s^{-1}, respectively. In general, the strain-hardening ability in metallic materials gradually diminishes with increasing deformation temperature owing to the activation of restoration phenomena such as dynamic recovery. One interesting observation in the present study was that two different regimes of the strain-hardening were realized with increasing temperature. The first regime was found in a temperature range from 25 °C to 300 °C, as indicated by the inset **a1** in Fig. 7a and the inset **b1** in Fig. 7b. That is, the strain-hardening curves at 25 °C and 100 °C were initially higher than that associated to 300 °C, mainly due to the promoted twinning activity at lower temperatures. But those strain-hardening curves dropped quickly with further straining and eventually they became lower than the strain-hardening rate at 300 °C. Once such strain-hardening degradation happened, it could lead to the plastic instability. As a result, a moderate decrease in the fracture strain in the temperature range from 300 °C to 25 °C was observed, as previously shown (Figs. 2, 3c). Note that Cantor alloy shows a different mechanical response in the tensile deformation (up to small strains < 1.0). That is, the HEA exhibits enhancement in the strain-hardening and the ductility (Fig. 3d) due to the promotion of twin activity at low temperatures [5–7,11]. In the high-strain torsion, we suggest that the accelerated decline in the strain-hardening ability (despite extensive twinning) and the resultant decrease in ductility are related to the shear localization operated at moderate to large strains (**Fig. S2b-d** in supplementary materials). From a microstructural viewpoint, the HEA undergoes extensive grain refinement down to nano-meter scales (Fig. 4g). Accordingly, homogeneous deformation in the strain-hardened matrix of the refined microstructure becomes difficult, and then strain localization in the form of shear band takes over as the main de-

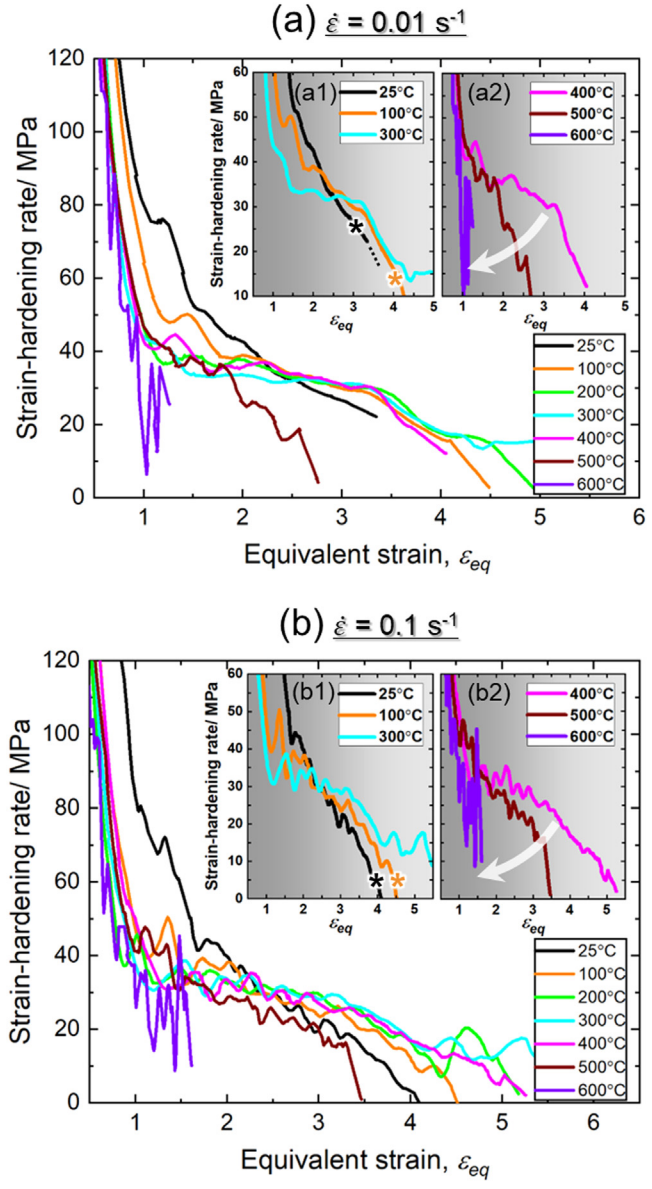

Fig. 7. Strain-hardening rate ($\partial\sigma/\partial\varepsilon$) plotted as a function of equivalent strain at various deformation temperatures ranging from 25 °C to 600 °C. The graphs in (a) and (b) are associated with the deformation at strain rates of 0.01 s^{-1} and 0.1 s^{-1}, respectively. Each graph includes two insets representing two different tendencies of the strain-hardening over temperature ranges of 25 °C-300 °C (a1, b1) and 400 °C-600 °C (a2, b2). The plots marked by asterisks in (a1) and (b1) indicate that a temperature rise caused by the plastic deformation was detected during the torsion tests.

formation mode under the high-strain deformation [26,35]. Shear band development is usually undesirable as it leads to the plastic instability followed by the fracture of metals [36]. To prove our speculation, we conducted an additional experiment to compare the degree of shear localization in two specimens that were highly deformed ($\varepsilon \sim 4.2$) at temperatures of 25 °C and 300 °C. The results are shown in **Fig. S5** in supplementary materials. It was found that the deformation microstructure at 25 °C contained numerous macro-scale shear bands that led to large cracks propagating and eventually failure of the specimen deformed at 25 °C. Comparatively, the degree of shear localization at 300 °C was much weaker than that at 25 °C, leading to the better deformability (higher fracture strain) of the specimen deformed at 300 °C.

The other strain-hardening regime corresponded to the deformation in a temperature range from 400 °C to 600 °C, as shown by insets **a2** and **b2** in Fig. 7. Under this regime, increasing temperature to 600 °C resulted in an accelerated drop in the strain-hardening plots, which was soon followed by the early fracture of the specimens. This observation can be interpreted from two different perspectives. (1) The lack of strain-hardening capacity might be attributed to the suppression of the twinning mechanism at elevated temperatures. However, the twinning activity in a temperature range of 400 °C-600 °C did not seem to be fundamentally changed (Figs. 5, 6), so that the insufficient deformation twinning was probably not responsible for the early fracture in the temperature range[1]. (2) We propose that the formation and coalescence of micro-voids at GBs (Fig. 6e-f) played the main role in declining the strain-hardening ability at 600 °C. The underlying mechanism to the micro-void formation and early failure at 600 °C is discussed in the next section.

3.4. Intermediate-temperature embrittlement in HEA

3.4.1. Fracture surface analysis

To understand the mechanism of the early fracture at intermediate temperatures, we firstly examined the fracture surface in the specimen failed at 600 °C ($\varepsilon_f = 1.3$). Additionally, the fracture surface in the specimen fractured at 100 °C ($\varepsilon_f = 4.5$) was observed and compared with the result obtained from the 600 °C deformation (Fig. 8). Figure 8a-**e** show micrographs of the fracture surfaces at 100 °C. Figure 8a is a low magnification SEM-image of the fracture surface viewed from the shear-plane-normal (SPN) direction in torsion. The grey arc arrows indicate the shear (rotation) direction in torsion. For reference, Fig. 8b displays the overall view of the fractured specimen after its gage part split in half along the macroscopic shear plane. Note that due to the strain gradients in the circular cross-section of the gage part, usually cracks initiated from the outer side of the circular section that was more deformed, and then cracks propagated towards the center until the complete fracture occurred. Figure 8c represents the fracture surface near the outer side of the circular section. This part was, however, severely damaged because the opposite sides of the fracture surfaces could slide over each other due to the rotational movement in torsion. Nevertheless, the surface damage was negligible close to the center part, and the surface in this region could be appropriately analyzed (Fig. 8d, 8e). The micrographs displayed dimple patterns suggesting that a ductile manner of fracture occurred at 100 °C. The surface morphologies exhibited fine and coarse dimples, while the coarse dimples often contained particles inside. Such particles or inclusions do often exist in the CoCrFeMnNi HEAs that are fabricated during melting and casting processes [5,37]. They appear to be oxide particles enriched in Mn or Cr (Suppl. **Fig. S7**). Both elements are strong oxide formers [38,39].

Figure 8f-**j** shows micrographs of the fracture surfaces in the specimen susceptible to the early fracture at 600 °C. The fracture surface normal to the shear plane in torsion (Fig. 8f) and the over-

[1] In order to prove that the early fracture at 600 °C was not related to the suppression of twin activities and lack of strain-hardening ability, we conducted an additional experiment of which details are provided as Supplementary materials (**Fig. S6**). First, a specimen was deformed at 200 °C, where the material showed an excellent ductility and strain-hardening ability owing to the profound twin-induced plasticity at such a low temperature. Another specimen was initially processed (pre-deformed and aged) at 600°C and subsequently deformed at 200°C. It was found that the pre-processed specimen showed a clear degradation of ductility even though the specimen was deformed at the same temperature of 200°C with similar strain-hardening behavior as that of the first specimen. This observation suggests that the early fracture at intermediate temperatures is caused by other reason different from the suppressed strain-hardening ability with increasing temperature.

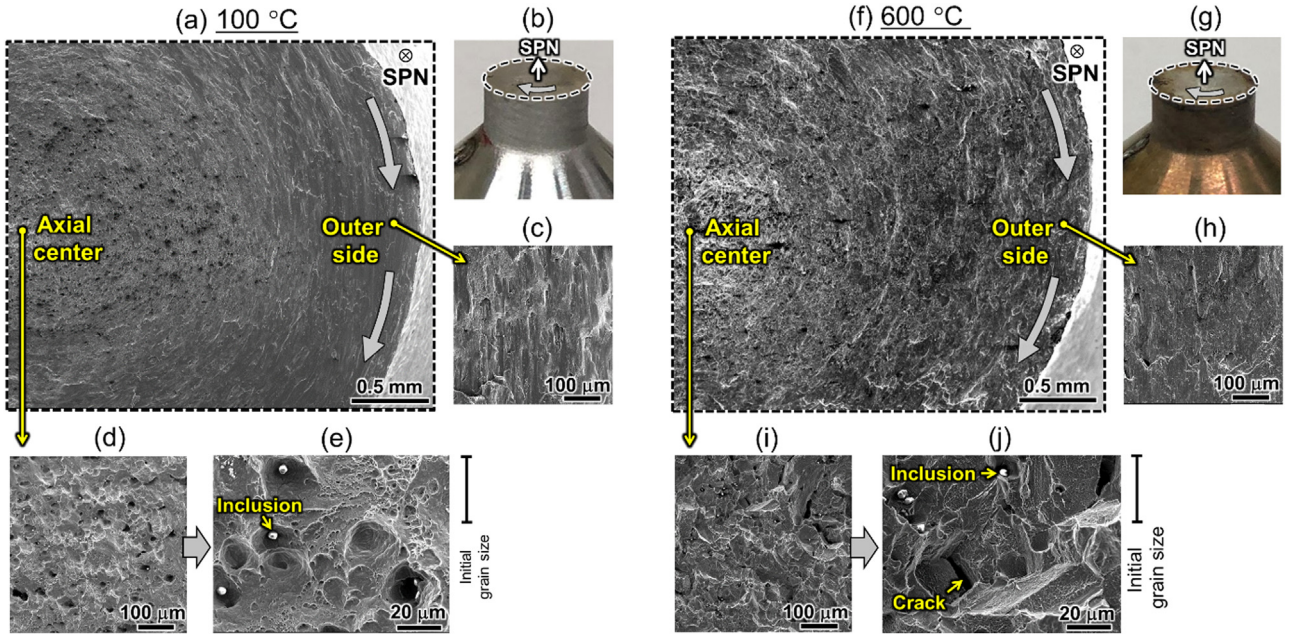

Fig. 8. SEM micrographs showing fracture surfaces in the specimens fractured at (a-e) 100 °C ($\varepsilon_f = 4.5$, $\dot{\varepsilon} = 0.01\ s^{-1}$) and (f-j) 600 °C ($\varepsilon_f = 1.3$, $\dot{\varepsilon} = 0.01\ s^{-1}$). (a, f) Low-magnification images of the fractured surfaces viewed from the shear plane normal (SPN) in torsion. The grey arc arrows indicate the shear (rotation) direction in torsion. (b, g) Overall views of the fractured specimens in torsion, (c, h) enlarged fracture surfaces close to the outer sides of the circular cross-sections, and (d-e, i-j) enlarged fracture surfaces close to the center of the circular sections, in the specimens fractured at 100 °C and 600 °C respectively.

all view of the fractured specimen (Fig. 8g) are provided. As previously described, the fracture surface in the outer side of the circular cross-section was significantly damaged by sliding (Fig. 8h). Near the center part, the fracture surface exhibited prominent facet-like morphologies (Fig. 8i, 8j). These patterns were different from the dimple patterns found in the specimen fractured at 100°C (Fig. 8d, 8e). The facet sizes were comparable to the average grain size in the initial microstructure. A reference scale representing the initial grain size is provided in Fig. 8j. It should be noted that in torsion deformation the center regions (initial grains) are not deformed by shear so much theoretically. Deep cracks caused by GB decohesion could be found on the surface (Fig. 8j). These results suggest that cracks preferentially propagated along initial GBs, leading to intergranular fracture at 600 °C. This assessment was in agreement with the microstructure observation shown in Fig. 6f, where the formation and coalescence of micro-voids at initial GBs were often found in the microstructure. Note that the size and distribution of inclusions appeared on the fracture surface at 600 °C were the same as those found at 100 °C. Thus, the presence of inclusions could not cause a difference in the fracture modes of the specimens. Another factor must play a role in the intergranular fracture at 600 °C, as will be shown later.

3.4.2. Grain boundary precipitation

We furthermore examined the specimen deformed at 600 °C by employing HAADF (high-angle annular dark field) imaging and EDS analysis in STEM mode. Figure 9**a** is a HAADF-STEM image representing an initial grain boundary region and Fig. 9b is the corresponding BF micrograph. There existed nano-size precipitates decorating the GB. No evidence of such precipitation could be found in the specimens processed at 100 °C and 400 °C (Figs. 4, 5). Figure 9c-g represents the elemental mappings by STEM-EDS taken from the GB region shown in Fig. 9a. The precipitates were enriched in Cr, as indicated in Fig. 9c. Additionally, there were heterogeneous distributions of elements (lean and rich spots) in the EDS maps suggesting that alloying elements could segregate and redistribute along the GB. Figure 9h is a high-magnification bright-field image showing a Cr-rich precipitate nucleated at the GB. Based on the EDS analysis, the average chemical composition of the precipitate contained 42.5% Cr together with 18.5% Co, 18.9% Fe, 12.5% Mn, and 7.6% Ni (in at.%). Figure 9j represents a SAD pattern obtained from the precipitate along a low-index crystal axis [111] parallel to the electron beam. It was found that the crystal structure of the precipitate was tetragonal with lattice parameters of $a \sim 4.6$ Å and $c \sim 8.8$ Å. Both chemical composition and crystallographic data of the Cr-rich phase were consistent with the characteristics of σ phase previously reported in Cantor alloy and Cr-containing steels [40–42].

Figure 10 represents the result of APT analysis from an initial GB region in the specimen deformed at 600 °C. Fig. 10a illustrates 3D-reconstruction of elements in the APT sample. Note that there existed a trace amount of impurities such as Si ($<$ 100 ppm) in the HEA. The Si atoms, as illustrated in Fig. 10b, were segregated along the GB, therefore Si atoms were used for better visualization of the GB alignment in the APT sample. Figure 10c and 10d demonstrate atom maps of Cr and Mn including iso-composition surfaces of 23 at% Cr and 23 at% Mn, respectively. As highlighted by purple-color regions in Fig. 10c, Cr-rich nanoclusters intended to form at the GB while other regions adjacent to the GB became enriched in elements such as Mn and formed Mn-rich nanoclusters, as shown by green-color regions in Fig. 10d. Such elemental partitioning along the GB could affect the GB cohesion and, therefore, mechanical properties of the HEA subjected to the intermediate-temperature deformation. Nanoclustering of the elements could also provide precursors for the nucleation of secondary phases such as Cr-rich phases, as shown in Fig. 9.

It is known that the FCC solid solution in the CoCrFeMnNi HEA is a meta-stable phase at temperatures below 800 °C $\sim$ 850 °C [41–43]. It has been reported that upon annealing at 700 °C, the HEA forms precipitates known as Cr-rich σ-phase having a tetragonal structure [41,42]. Annealing at a low temperature of 500 °C results in the decomposition of the FCC matrix into several phases such as BCC-Cr phase, NiMn-rich phase ($L1_0$ structure), and FeCo-rich phase (B2 structure) [41]. The phase decomposition is slow

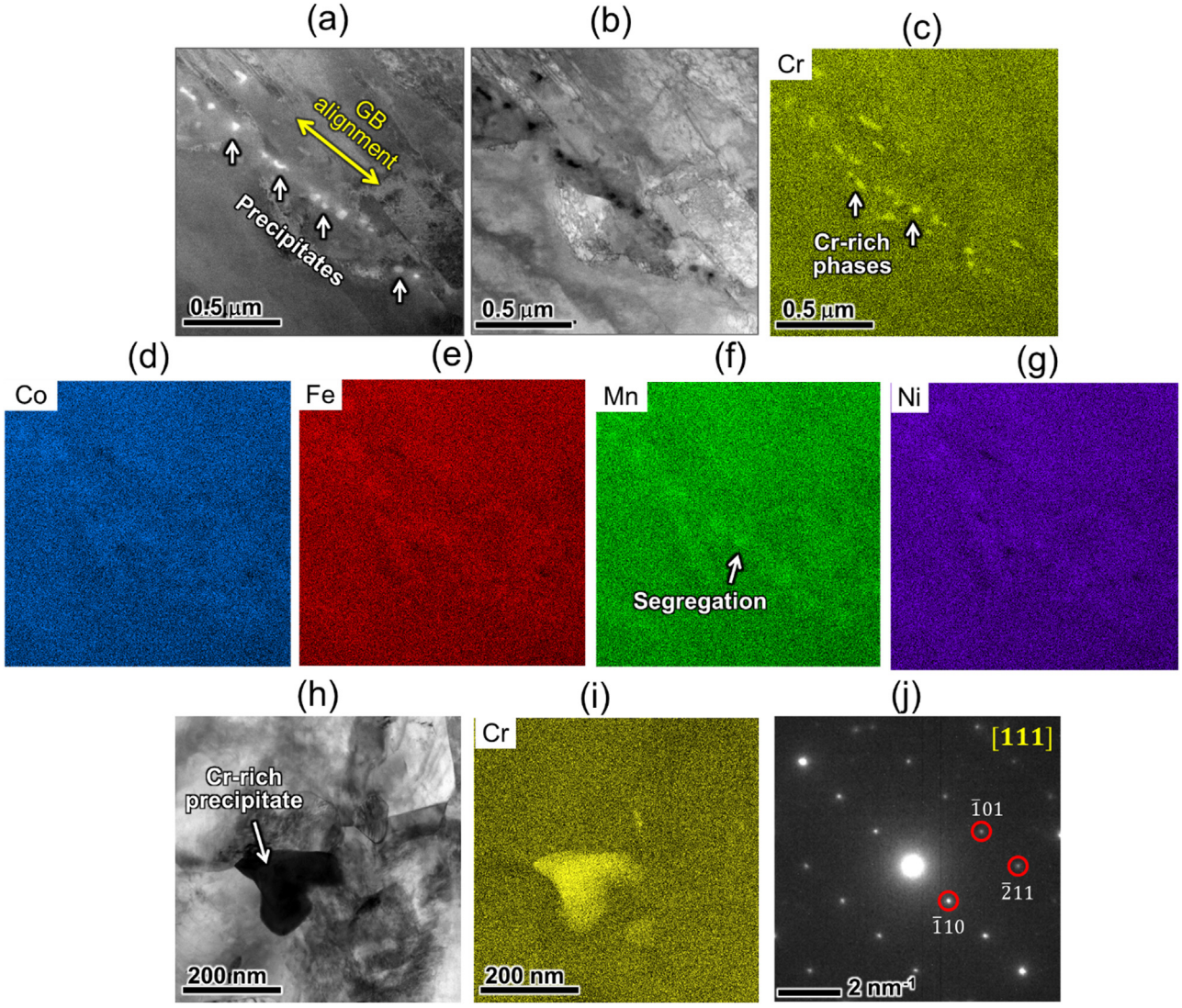

Fig. 9. Precipitation along initial grain boundary in the specimen deformed at 600 °C (ε_f = 1.3, $\dot{\varepsilon}$ = 0.01 s^{-1}). (a) HAADF (high-angle annular dark field)-STEM image taken from an initial GB region and (b) corresponding bright-field image. (c-g) STEM-EDS elemental mappings from the same area shown in (a). The mapped elements are shown in the figures. (h) High-magnification bright-field image showing a Cr-rich precipitate nucleated at the grain boundary, (i) corresponding EDS mapping of Cr, and (j) representative SAD pattern of the precipitate shown in (h) obtained along [111] zone axis.

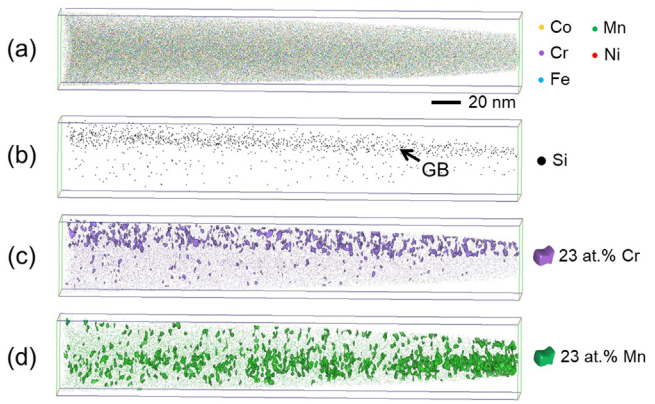

Fig. 10. APT analysis from an initial grain boundary region in the CoCrFeMnNi HEA subjected to the torsion deformation at 600 °C (ε_f = 1.3, $\dot{\varepsilon}$ = 0.01 s^{-1}). (a) 3D-reconstruction of atoms in the needle-shape APT sample. (b) Elemental map of Si showing that Si atoms were decorated along the grain boundary. (c, d) Elemental maps of Cr and Mn together with iso-composition surfaces of 23 at% Cr (purple-color regions) in (c) and 23 at% Mn (green-color regions) in (d).

upon static annealing of an undeformed HEA, and it may take several hundred hours to form such precipitates [41,42]. As a result, the CoCrFeMnNi HEA often maintains its single-phase FCC structure upon cooling from high temperatures to ambient temperature. However, Schuh et al. [17] have reported that the FCC matrix of a severely deformed HEA quickly decomposes and forms precipitates upon subsequent annealing at temperatures below 800 °C. It seems that the large numbers of grain boundaries and lattice defects introduced by severe plastic deformation facilitate the elemental diffusion leading to the quick phase separation in the FCC phase. Later on, several researchers used the plastic deformation prior to annealing as a strategy to fabricate precipitate-containing CoCrFeMnNi HEAs [18,44–47]. The present study provides direct evidence that precipitation in initial GB regions can happen during the deformation at elevated temperatures (Fig. 9). We consider that the dislocation substructures and lattice defects that form adjacent to initial GBs accelerate the elemental diffusion into the GBs. The high concentrations of segregated elements can lead to the precipitation at the GBs.

Segregation and GB precipitation are often undesirable phenomena for mechanical properties of metallic materials. Ming et al.

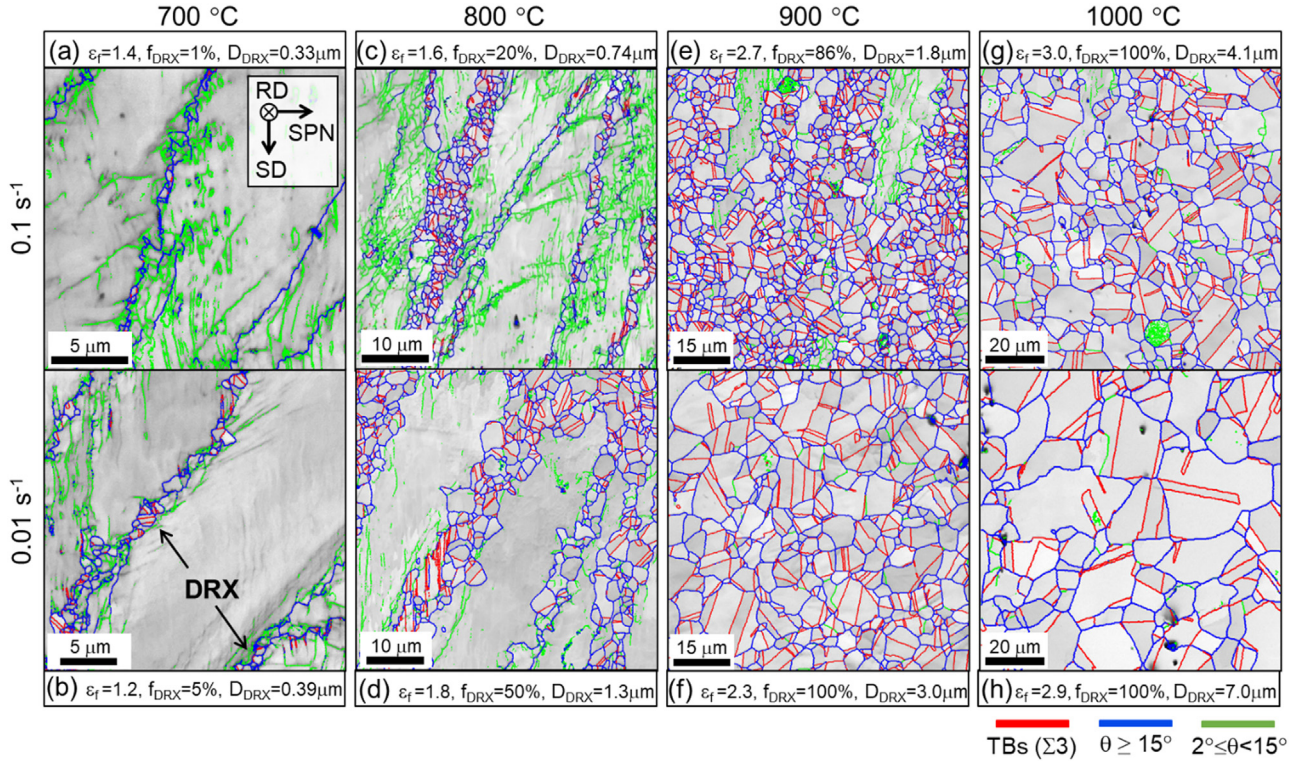

Fig. 11. EBSD boundary maps (overlaid on image quality maps) representing microstructures of the CoCrFeMnNi HEA deformed to fracture at temperatures of (a, b) 700 °C, (c, d) 800 °C, (e, f) 900 °C, and (g, h) 1000 °C. Different strain rates of 0.1 s^{-1} (upper row) and 0.01 s^{-1} (lower row) were applied for the deformation. Red, blue, and green lines indicate annealing twin boundaries (Σ3), high angle boundaries ($\theta \geq 15°$), and low angle boundaries ($2° \leq \theta < 15°$), respectively. All microstructures are viewed from the radial direction (RD) normal to the SPN-SD plane. SPN and SD are the shear plane normal and shear direction in torsion, respectively.

[21] have reported GB segregations of principal elements Cr, Mn, and Ni in the CoCrFeMnNi HEA subjected to tensile loading at intermediate temperatures. They have suggested that the segregation promotes GB decohesion leading to ductility loss that often observed in tensile testing of the HEA at intermediate temperatures (Fig. 3d). Employing APT analysis, Li et al. [48] have reported spinodal-like elemental redistributions within the segregated GB region. The phenomenon may provide precursors to the nucleation of new phases, like the Cr-rich phases found in the current study (Fig. 9). In fact, the Cr-rich precipitates are considered as σ phases according to the temperature range they form [18,41–47]. Besides, chemical composition of the precipitates and their tetragonal crystal structure (Fig. 9j) very well match the characteristics of σ phase reported in literature [40–42]. σ phases are commonly found in Cr-containing stainless steels, in which brittle σ precipitates are detrimental to the mechanical properties of stainless steels [49]. Jo et al. [50] have studied a quaternary $V_{20}Cr_{15}Fe_{20}Ni_{25}$ alloy having FCC matrix with σ-precipitates at the GBs. They have reported formations of micro-voids and cracks at σ/FCC-matrix interfaces upon tensile loading. Accordingly, we conclude that the intergranular fracture leading to the less deformability of the current CoCrFeMnNi is attributed to the nanoprecipitation of σ particles at initial GBs. In future application, hot deformation at such temperatures should be avoided for the CoCrFeMnNi HEA.

3.5. Deformation microstructures at $T > 600$ °C

We showed that the strength of the HEA above 600 °C quickly decreased with increasing deformation temperature (Fig. 3a). Additionally, the flow stress at high temperatures reached the maximum value and then underwent softening until fracture occurred (Fig. 2). The type of microstructure evolution contributed to such mechanical responses is discussed here.

Figure 11 represents EBSD boundary maps of the CoCrFeMnNi HEA deformed in a temperature range from 700 °C to 1000 °C, using different strain rates of 0.1 s^{-1} (upper row) and 0.01 s^{-1} (lower row). All microstructures are shown at their fracture strains (ε_f). The amount of ε_f at each deformation condition is stated in Fig. 11, where ε_f increased from ~1.2 at 700 °C to ~3.0 at 1000 °C. It can be seen that dynamic recrystallization (DRX) occurred in the microstructures, and the DRX became more and more dominant with increasing temperature. Microstructures deformed at lower temperatures such as 700 °C and 800 °C were partially recrystallized (Fig. 11a-**e**). Those microstructures were composed of deformed initial grains that were elongated along SD and new DRX grains that formed preferentially along initial GBs. Fractions and sizes of the DRX grains (f_{DRX}, D_{DRX}) increased with increasing temperature and decreasing strain rate, which is a typical tendency of DRX in hot deformation. Fully recrystallized microstructures were found at temperatures above 800 °C (Fig. 11f-h). Here, the faster DRX kinetics at higher temperatures and the larger applied strains ($\varepsilon > 2$) led to the completion of DRX in the corresponding microstructures. Abundant annealing twins with Σ3-type boundaries illustrated by the red line in Fig. 11 were involved in the DRX grains.

Figure 12 demonstrates nucleation and growth stages of DRX in the HEA. Figure 12a is an IPF map representing a nucleation stage at a pre-existing high-angle grain boundary. Red, black, and gray lines in the EBSD IPF map indicate annealing twin boundaries (Σ3), high angle boundaries ($\theta \geq 15°$), and low angle boundaries ($2° \leq \theta < 15°$), respectively. Serrations on the pre-existing GB were developed due to movement of the GB along substructures that formed in the neighboring grains (G1, G2). DRX nuclei first appeared at the pre-existing GB, like the nuclei N1 and N2 marked by circles in Fig. 12a. Some parts of the serrated GB could bulge into the deformed matrix with a driving force caused by the difference in dislocation density across the boundary. Free-dislocation

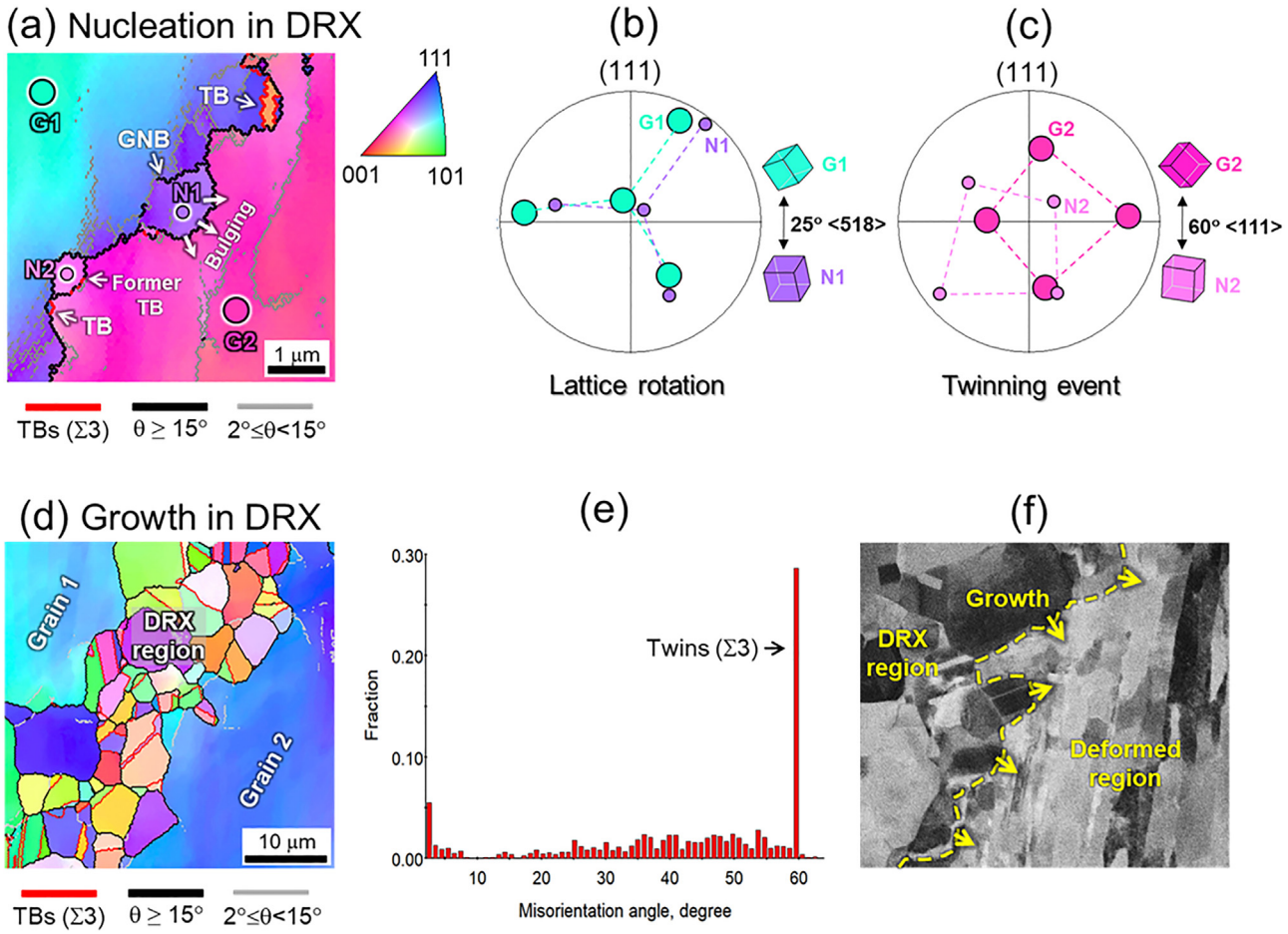

Fig. 12. Evolution of DRX in the CoCrFeMnNi HEA. (a) IPF map showing the nucleation of DRX grains at a pre-existing high-angle grain boundary. Nuclei N1 and N2 and parent grains G1 and G2 are marked by circles in (a) for the orientation analysis. (b, c) (111) pole figures showing the crystallographic orientation relationships between the nuclei and the parent grains for the pairs of (G1, N1) shown in (b) and (G2, N2) shown in (c), respectively. Crystal frames are shown for better visualization. Notations related to the rotation angle and <rotation axis> are provided. (d) IPF map showing the growth stage of the DRX. (e) Distribution of misorientation angle across the boundaries in the microstructure shown in (d). (f) SEM-BSE image showing the growth of DRX grains into the deformed region. Red, black, and gray lines in IPF maps (a, d) indicate annealing twin boundaries (Σ3), high angle boundaries ($\theta \geq 15°$), and low angle boundaries ($2° \leq \theta < 15°$), respectively.

regions that left behind the migrating pre-existing boundaries (nuclei) were enclosed by the newly-formed boundaries that separated the nuclei (N1, N2) from the parent grains (G1, G2). For the nucleus N1, a geometrically necessary boundary (GNB) formed and separated N1 from the parent grain G1. The orientation relationship between N1-G1 is illustrated by a (111) pole figure in Fig. 12b. Crystal frames in N1 and G1 are provided for better visualization. Note that due to the strain incompatibility at the pre-existing GB, the lattice rotation near the GB region can be accelerated. The lattice rotation assists the nucleation process by providing GNBs with high-angle misorientations (>15°). For the nucleus N2, an annealing twinning event was involved in the nucleation stage. Figure 12c shows the orientation relationship between the nucleus N2 and the parent grain G2. Note that annealing twins can lose their coherent boundaries (Σ3 type: 60°<111>) soon after they form. That is, they become normal high angle boundaries, as it likely happened in the nucleation of N2 shown in Fig. 12a. Nucleation mechanisms similar to those found in the HEA have been reported in hot deformation of FCC metals having low SFE such as Copper and Ni-30%Fe [51–53].

Figure 12d exhibits a later stage of DRX, where the DRX region had expanded into two neighboring grains. Figure 12e shows the distribution of boundary misorientation corresponding to the microstructure shown in Fig. 12d. A large fraction of annealing twins with the misorientation angle of 60° could be realized in the profile. In other words, annealing twin formations were frequently involved in the growth stage of DRX. A SEM-BSE image in Fig 12d provides details of the growth stage. A recrystallized region having several equiaxed grains existed in the vicinity of a deformed region having a typical banded substructure. Strain-free DRX grains could grow into the deformed region and eliminate the strain-hardened matrix to reduce the stored energy in the deformed material. Such a restoration process led to the quick softening of the HEA that was observed at temperatures above 600 °C (Fig. 3a).

We assessed the growth behavior in the CoCrFeMnNi HEA and other FCC materials by comparing their DRX grain sizes (D_{DRX}) obtained in hot deformation. The results are summarized in Fig. 13, where D_{DRX} is plotted as a function of the normalized temperature (T/T_m: homologous temperature, where Tm is the melting temperature of the material) at constant strain rates. Figure 13a represents D_{DRX} data obtained in the current HEA and a 18Cr-8Ni austenitic stainless steel we previously studied, deformed by hot torsion [54]. It should be mentioned that twin boundaries were included in the grain size measurements. The DRX grain sizes in the HEA were relatively smaller than those in the austenitic stainless steel. The smaller D_{DRX} in the HEA was partly originated from its larger fractions of twins compared to those in the austenitic stainless steel (Suppl. **Fig. S8**). For comparison, Fig. 13b demonstrates D_{DRX} data reported in the literature on the CoCrFeMnNi HEAs [55,56] and other FCC materials, i.e., 18Cr-8Ni austenitic stainless steel [57], Ni-

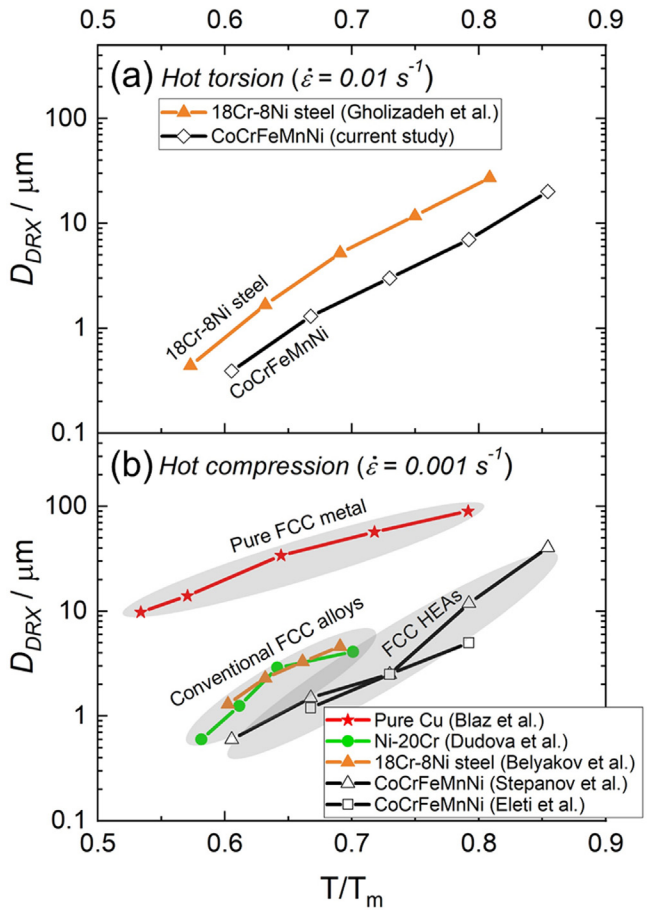

Fig. 13. DRX grain sizes (D_{DRX}) in the CoCrFeMnNi HEA and different FCC materials, plotted as a function of the homologous deformation temperature. The horizontal axis is the deformation temperature normalized by melting points in different materials. (a) D_{DRX} data obtained in hot torsion of the CoCrFeMnNi HEA in the current study and a 18Cr-8Ni austenitic stainless steel deformed by hot torsion in our previous study [54]. (b) D_{DRX} data obtained in hot compression of the CoCrFeMnNi HEAs [55,56] and different FCC materials [57–59]. The materials were deformed at constant strain rates of (a) 0.01 s^{-1} in torsion and (b) 0.001 s^{-1} in compression.

20Cr [58], and pure Copper [59], deformed by hot compression. In general, DRX and grain growth in pure metals are fast and lead to large DRX grain sizes, similar to those reported for the pure Copper (Fig. 13b). Adding alloying elements can retard the GB mobility and growth, which results in the smaller grain sizes in conventional FCC alloys and FCC HEAs. In Fig. 13b, the D_{DRX} plots of the HEAs were smaller than those of conventional FCC alloys, in agreement with the results in Fig. 13a. It has been claimed that the diffusion in HEAs is sluggish owing to a high number of principal elements [60]. Therefore, the grain growth, which is a diffusion-assisted phenomenon might become slower, leading to smaller D_{DRX} in the HEAs compared to the conventional alloys. However, increasing the number of alloying elements also decreases the melting temperature of the HEAs (higher T/Tm), which has an impact on the plots in Fig. 13. In fact, at the same temperature (T), D_{DRX} of the HEAs became closer to D_{DRX} of the conventional alloys (Suppl. **Fig. S9**). Overall, we realized only a moderate decrease in the DRX grain sizes of the HEA, instead of substantial refinement in D_{DRX} that would be expected to happen owing to the sluggish diffusion in the HEA. The results shown in Fig. 13 support recent assessments that the diffusion in the HEA is not fundamentally slower than the diffusion in conventional alloys [61–63].

3.6. Importance of the present results

In order to provide an overall understanding of the metal-working process in the novel CoCrFeMnNi HEA, the torsion deformation of the HEA at different temperatures was investigated in the present study. We systematically discussed mechanical responses and their correlation with deformation microstructures at various temperatures. The present work can provide a guide for controlling microstructures of the CoCrFeMnNi HEA through thermomechanical processing. Here, it is worth mentioning some important points clarified in the current study. Providing high strains in torsion, twinning activity in the HEA extends from room temperature to temperatures as high as ~ 600°C (Figs. 4-6). The HEA has decent deformability at low temperatures (up to 400 °C, Fig. 2) owing to the twin-induced (and microband-induced) plasticity. However, localized shear deformation that can degrade the deformability to some extent must be taken into consideration. Localized shear deformation can be intensified at high strains, low deformation temperatures, and high strain rates [64]. Outmost attention should be given to the phase stability of the FCC solid solution processed at temperatures below 800 °C [41,42]. Decomposition of the solid solution into secondary phases can be accelerated by applying plastic strain at elevated temperatures. The CoCrFeMnNi HEA shows a susceptibly to the intergranular fracture (Figs. 3c, 8f-j) caused by GB precipitation of Cr-rich σ phases in a temperature range from 600 °C to 800 °C (Fig. 9). We suggest that any processing of the HEA at these intermediate temperatures (deformation, aging heat treatment, etc.) should be avoided or kept as minimum as possible (Suppl. **Fig. S6**). Apart from the deformability viewpoint, the precipitation of secondary phases might be beneficial to some practical applications, such as improving the wear-resistance performance of the CoCrFeMnNi HEA [65]. It is recommended that hot working of the HEA, such as hot rolling and forging, should be conducted at temperatures above 800°C, where the HEA maintains its single-phase structure and shows adequate deformability. Additionally, controlling temperature and strain rate can be effectively used to fabricate various DRX microstructures in the HEA with desired grain sizes (Fig. 11). DRX in the concentrated solid solution of the CoCrFeMnNi HEA (Figs. 12, 13) does not seem to be fundamentally different from that in conventional FCC materials with relatively low stacking fault energies.

4. Summary and conclusions

The purpose of the current study was to give a global view on the temperature-dependence of plasticity and deformation microstructures in CoCrFeMnNi Cantor alloy by covering a wide range of strains that could not be achieved by conventual deformation. Accordingly, an equi-atomic CoCrFeMnNi was deformed by high-strain torsion to von Mises equivalent strains (ε) of 1~5.5 in a temperature range from 25 °C to 1100 °C. Mechanical responses of the HEA greatly varied depending on the types of microstructure evolution at different temperatures. The main findings of the study are summarized as follows:

(1) Temperature-dependence of strength and deformability in torsion deformation of the HEA were evaluated systematically. The strength (defined as the equivalent stress at the fracture point in torsion) decreased slowly with increasing temperature up to 600 °C. Then, the strength dropped quickly at temperatures above 600 °C since softening by DRX occurred. The deformability of the HEA showed various tendencies. That is, the maximum fracture strains of ε_f = 4.0~5.5 were achieved at low temperatures (25 °C~400 °C), then the fracture strain dramatically dropped to ε_f = 1.2~1.3 at intermediate temperatures (600 °C~700 °C). The deformability was enhanced again, and

the fracture strains reached 2.0∼3.0 at high temperatures (> 800 °C).

(2) The excellent deformability at low temperatures was attributed to the profound twin-induced plasticity as well as microband-induced plasticity. The formation of thick twin bundles composed of finely-spaced nanotwins, localized shear bands, and microbands at 100 °C as well as the formation of nanotwins and microbands at 400 °C were the common microstructural features in the low-temperature deformation. Deformation twinning could be extensively activated at moderate strains ($\varepsilon \sim 1$) and extended to ultrahigh strains (4.0 ∼5.5) until fracture occurred. The HEA underwent extensive grain refinement and nanostructured lamellae having grain sizes of 50 nm∼150 nm were obtained by the deformation to ultrahigh strains.

(3) The HEA exhibited high strain-hardening due to increasing fractions of interfaces (nanotwins and microbands) that could act as obstacles to the dislocation glide (dynamic Hall-Petch effect). However, two phenomena could negatively affect the work-hardening behavior and thus the deformability of the HEA: (a) localized shear deformation intensified by the high straining at low temperatures (< 300 °C), and (b) formation of defects such as micro-voids promoted by the deformation at intermediate temperatures (≥ 500 °C).

(4) A distinctive embrittlement was realized at intermediate temperatures (600 °C∼800 °C) since the fracture strains reduced substantially by more than 70% compared to those at low temperatures. Formation and coalescence of the micro-voids at pre-existing GBs were often observed in the microstructures of the failed specimens. Additionally, fracture surfaces showed facet-like morphologies and promotion of the intergranular cracks. The susceptibility to the micro-void formation and intergranular fracture was due to the formation of nano-sized precipitates (Cr-rich σ-phases) along the pre-existing GBs. Dislocation substructures induced by the plastic deformation could assist the elemental segregation to the GBs and accelerate the GB precipitation.

(5) The HEA underwent softening caused by DRX at temperatures above 600 °C. The deformability was enhanced again, which could be related to the DRX activation, and the fact that the HEA could maintain its single-phase structure (no GB precipitation) at temperatures above 800 °C. Fractions and sizes of DRX grains increased with increasing the temperature and decreasing the strain rate. Ultrafine and fine-grained DRX microstructures (0.3 μm∼20 μm) could be obtained by the deformation at high temperatures. Nucleation of DRX grains and their average sizes in the HEA did not seem to be considerably different from those in conventional FCC materials having low stacking fault energy.

Declaration of Competing Interest

The authors declare that they have no known competing financial interests or personal relationships that could have appeared to influence the work reported in this paper.

Acknowledgments

This study was financially supported by the Grant-in-Aids for Scientific Research (S) (No.JP15H05767), the Grant-in-Aid for Scientific Research (A) (No.JP20H00306), the Grant-in-Aid for Scientific Research on Innovative Area “High Entropy Alloys” (No.JP18H05455), the Elements Strategy Initiative for Structural Materials (ESISM, No.JPMXP0112101000), and JST CREST (No.JPMJCR1994) all through the Ministry of Education, Culture, Sports, Science and Technology (MEXT), Japan. The supports are gratefully appreciated by the authors.

Supplementary materials

Supplementary material associated with this article can be found, in the online version, at doi:10.1016/j.actamat.2022.118514.

References

[1] J.W. Yeh, S.K. Chen, S.J. Lin, J.Y. Gan, T.S. Chin, T.T. Shun, C.H. Tsai, S.Y. Chang, Nanostructured high-entropy alloys with multiple principal elements: novel alloy design concepts and outcomes, Adv. Eng. Mater. 6 (2004) 299–303, doi:10.1002/adem.200300567.

[2] B. Cantor, I.T.H. Chang, P. Knight, A.J.B. Vincent, Microstructural development in equiatomic multicomponent alloys, Mater. Sci. Eng. A. 375–377 (2004) 213–218, doi:10.1016/j.msea.2003.10.257.

[3] E.P. George, W.A. Curtin, C.C. Tasan, High entropy alloys: a focused review of mechanical properties and deformation mechanisms, Acta Mater. 188 (2020) 435–474, doi:10.1016/j.actamat.2019.12.015.

[4] Z. Lyu, X. Fan, C. Lee, S.Y. Wang, R. Feng, P.K. Liaw, Fundamental understanding of mechanical behavior of high-entropy alloys at low temperatures: a review, J. Mater. Res. 33 (2018) 2998–3010, doi:10.1557/jmr.2018.273.

[5] A. Gali, E.P. George, Tensile properties of high- and medium-entropy alloys, Intermetallics 39 (2013) 74–78, doi:10.1016/j.intermet.2013.03.018.

[6] F. Otto, A. Dlouhý, C. Somsen, H. Bei, G. Eggeler, E.P. George, The influences of temperature and microstructure on the tensile properties of a CoCrFeMnNi high-entropy alloy, Acta Mater. 61 (2013) 5743–5755, doi:10.1016/j.actamat.2013.06.018.

[7] S.J. Sun, Y.Z. Tian, H.R. Lin, X.G. Dong, Y.H. Wang, Z.J. Wang, Z.F. Zhang, Temperature dependence of the Hall–Petch relationship in CoCrFeMnNi high-entropy alloy, J. Alloys Compd. 806 (2019) 992–998, doi:10.1016/j.jallcom.2019.07.357.

[8] J.H. Kim, K.R. Lim, J.W. Won, Y.S. Na, H.S. Kim, Mechanical properties and deformation twinning behavior of as-cast CoCrFeMnNi high-entropy alloy at low and high temperatures, Mater. Sci. Eng. A. 712 (2018) 108–113, doi:10.1016/j.msea.2017.11.081.

[9] M.J. Jang, S. Praveen, H.J. Sung, J.W. Bae, J. Moon, H.S. Kim, High-temperature tensile deformation behavior of hot rolled CrMnFeCoNi high-entropy alloy, J. Alloys Compd. 730 (2018) 242–248, doi:10.1016/j.jallcom.2017.09.293.

[10] J.X. Fu, C.M. Cao, W. Tong, Y.X. Hao, L.M. Peng, The tensile properties and serrated flow behavior of a thermomechanically treated CoCrFeNiMn high-entropy alloy, Mater. Sci. Eng. A. 690 (2017) 418–426, doi:10.1016/j.msea.2017.03.031.

[11] G. Laplanche, A. Kostka, O.M. Horst, G. Eggeler, E.P. George, Microstructure evolution and critical stress for twinning in the CrMnFeCoNi high-entropy alloy, Acta Mater. 118 (2016) 152–163, doi:10.1016/j.actamat.2016.07.038.

[12] N.L. Okamoto, S. Fujimoto, Y. Kambara, M. Kawamura, Z.M.T. Chen, H. Matsunoshita, K. Tanaka, H. Inui, E.P. George, Size effect, critical resolved shear stress, stacking fault energy, and solid solution strengthening in the CrMnFeCoNi high-entropy alloy, Sci. Rep. 6 (2016) 1–10, doi:10.1038/srep35863.

[13] S. Huang, W. Li, S. Lu, F. Tian, J. Shen, E. Holmström, L. Vitos, Temperature dependent stacking fault energy of FeCrCoNiMn high entropy alloy, Scr. Mater. 108 (2015) 44–47, doi:10.1016/j.scriptamat.2015.05.041.

[14] A.J. Zaddach, C. Niu, C.C. Koch, D.L. Irving, Mechanical properties and stacking fault energies of NiFeCrCoMn high-entropy alloy, Jom 65 (2013) 1780–1789, doi:10.1007/s11837-013-0771-4.

[15] K.V.S. Thurston, A. Hohenwarter, G. Laplanche, E.P. George, B. Gludovatz, R.O. Ritchie, On the onset of deformation twinning in the CrFeMnCoNi high-entropy alloy using a novel tensile specimen geometry, Intermetallics 110 (2019) 106469, doi:10.1016/j.intermet.2019.04.012.

[16] S.J. Sun, Y.Z. Tian, H.R. Lin, H.J. Yang, X.G. Dong, Y.H. Wang, Z.F. Zhang, Transition of twinning behavior in CoCrFeMnNi high entropy alloy with grain refinement, Mater. Sci. Eng. A. 712 (2018) 603–607, doi:10.1016/j.msea.2017.12.022.

[17] B. Schuh, F. Mendez-Martin, B. Völker, E.P. George, H. Clemens, R. Pippan, A. Hohenwarter, Mechanical properties, microstructure and thermal stability of a nanocrystalline CoCrFeMnNi high-entropy alloy after severe plastic deformation, Acta Mater. 96 (2015) 258–268, doi:10.1016/j.actamat.2015.06.025.

[18] H. Shahmir, J. He, Z. Lu, M. Kawasaki, T.G. Langdon, Effect of annealing on mechanical properties of a nanocrystalline CoCrFeNiMn high-entropy alloy processed by high-pressure torsion, Mater. Sci. Eng. A. 676 (2016) 294–303, doi:10.1016/j.msea.2016.08.118.

[19] W. Wu, M. Song, S. Ni, J. Wang, Y. Liu, B. Liu, X. Liao, Dual mechanisms of grain refinement in a FeCoCrNi high entropy alloy processed by high pressure torsion, Sci. Rep. 7 (2017) 1–13, doi:10.1038/srep46720.

[20] D.S. Fields, W.A. Backofen, Determination of strain hardening characteristics by torsion testing, in: Proc ASTM, 1957, pp. 1259–1272, doi:10.1002/prca.201200064.

[21] K. Ming, L. Li, Z. Li, X. Bi, J. Wang, Grain boundary decohesion by nanoclustering Ni and Cr separately in CrMnFeCoNi high-entropy alloys, Sci. Adv. 5 (2019) eaay0639, doi:10.1126/sciadv.aay0639.

[22] Z. Wu, H. Bei, G.M. Pharr, E.P. George, Temperature dependence of the mechanical properties of equiatomic solid solution alloys with face-centered cubic crystal structures, Acta Mater. 81 (2014) 428–441, doi:10.1016/j.actamat.2014.08.026.

[23] J.-H. Min, Y.-U. Heo, S.-H. Kwon, S.-W. Moon, D.-G. Kim, J.-S. Lee, C.-H. Yim, Embrittlement mechanism in a low-carbon steel at intermediate temperature, Mater. Charact. 149 (2019) 34–40, doi:10.1016/j.matchar.2019.01.009.

[24] V. Laporte, A. Mortensen, Intermediate temperature embrittlement of copper alloys, Int. Mater. Rev. 54 (2009) 94–116, doi:10.1179/174328009X392967.
[25] L. Zheng, G. Schmitz, Y. Meng, R. Chellali, R. Schlesiger, Mechanism of intermediate temperature embrittlement of Ni and Ni-based superalloys, Crit. Rev. Solid State Mater. Sci. 37 (2012) 181–214, doi:10.1080/10408436.2011.613492.
[26] N. Kamikawa, N. Tsuji, Effect of deformation temperature on microstructure evolution in ARB processed ultralow carbon IF steel, Mater. Trans. 53 (2012) 30–37, doi:10.2320/matertrans.MD201115.
[27] D.A. Hughes, N. Hansen, D.J. Bammann, Geometrically necessary boundaries, incidental dislocation boundaries and geometrically necessary dislocations, Scr. Mater. 48 (2003) 147–153, doi:10.1016/S1359-6462(02)00358-5.
[28] D. Kuhlmann-Wilsdorf, N. Hansen, Geometrically necessary, incidental and subgrain boundaries, Scr. Metall. Mater. 25 (1991) 1557–1562, doi:10.1016/0956-716X(91)90451-6.
[29] N. Hansen, R.F. Mehl, A. Medalist, New discoveries in deformed metals, Metall. Mater. Trans. A. 32 (2001) 2917–2935, doi:10.1007/s11661-001-0167-x.
[30] D.A. Hughes, N. Hansen, High angle boundaries formed by grain subdivision mechanisms, Acta Mater 45 (1997) 3871–3886, doi:10.1016/S1359-6454(97)00027-x.
[31] Y.S. Li, Y. Zhang, N.R. Tao, K. Lu, Effect of the Zener–Hollomon parameter on the microstructures and mechanical properties of Cu subjected to plastic deformation, Acta Mater 57 (2009) 761–772, doi:10.1016/j.actamat.2008.10.021.
[32] C. Zener, J.H. Hollomon, Effect of strain rate upon plastic flow of steel, J. Appl. Phys. 15 (1944) 22–32, doi:10.1063/1.1707363.
[33] J. He, Q. Wang, H. Zhang, L. Dai, T. Mukai, Y. Wu, X. Liu, H. Wang, T.-G. Nieh, Z. Lu, Dynamic deformation behavior of a face-centered cubic FeCoNiCrMn high-entropy alloy, Sci. Bull. 63 (2018) 362–368, doi:10.1016/j.scib.2018.01.022.
[34] Z. Yang, M. Yang, Y. Ma, L. Zhou, W. Cheng, F. Yuan, X. Wu, Strain rate dependent shear localization and deformation mechanisms in the CrMnFeCoNi high-entropy alloy with various microstructures, Mater. Sci. Eng. A. 793 (2020) 139854, doi:10.1016/j.msea.2020.139854.
[35] D.A. Hughes, N. Hansen, Microstructure and strength of nickel at large strains, Acta Mater 48 (2000) 2985–3004, doi:10.1016/S1359-6454(00)00082-3.
[36] N. Yan, Z. Li, Y. Xu, M.A. Meyers, Shear localization in metallic materials at high strain rates, Prog. Mater. Sci. 119 (2021) 100755, doi:10.1016/j.pmatsci.2020.100755.
[37] A.J. Zaddach, R.O. Scattergood, C.C. Koch, Tensile properties of low-stacking fault energy high-entropy alloys, Mater. Sci. Eng. A. 636 (2015) 373–378, doi:10.1016/j.msea.2015.03.109.
[38] J.Y. He, C. Zhu, D.Q. Zhou, W.H. Liu, T.G. Nieh, Z.P. Lu, Steady state flow of the FeCoNiCrMn high entropy alloy at elevated temperatures, Intermetallics 55 (2014) 9–14, doi:10.1016/j.intermet.2014.06.015.
[39] G. Laplanche, U.F. Volkert, G. Eggeler, E.P. George, Oxidation behavior of the CrMnFeCoNi high-entropy alloy, Oxid. Met. 85 (2016) 629–645, doi:10.1007/s11085-016-9616-1.
[40] H.L. Yakel, Atom distributions in sigma phases. I. Fe and Cr atom distributions in a binary sigma phase equilibrated at 1063, 1013 and 923 K, Acta Cryst. B. 39 (1983) 20–28, doi:10.1107/S0108768183001974.
[41] F. Otto, A. Dlouhý, K.G. Pradeep, M. Kuběnová, D. Raabe, G. Eggeler, E.P. George, Decomposition of the single-phase high-entropy alloy CrMnFeCoNi after prolonged anneals at intermediate temperatures, Acta Mater 112 (2016) 40–52, doi:10.1016/j.actamat.2016.04.005.
[42] E.J. Pickering, R. Muñoz-Moreno, H.J. Stone, N.G. Jones, Precipitation in the equiatomic high-entropy alloy CrMnFeCoNi, Scr. Mater. 113 (2016) 106–109, doi:10.1016/j.scriptamat.2015.10.025.
[43] T.H. Chou, J.C. Huang, C.H. Yang, S.K. Lin, T.G. Nieh, Consideration of kinetics on intermetallics formation in solid-solution high entropy alloys, Acta Mater 195 (2020) 71–80, doi:10.1016/j.actamat.2020.05.015.
[44] W. Zhou, L.M. Fu, P. Liu, X.D. Xu, B. Chen, G.Z. Zhu, X.D. Wang, A.D. Shan, M.W. Chen, Deformation stimulated precipitation of a single-phase CoCrFeMnNi high entropy alloy, Intermetallics 85 (2017) 90–97, doi:10.1016/j.intermet.2017.02.010.
[45] N. Park, B.J. Lee, N. Tsuji, The phase stability of equiatomic CoCrFeMnNi high-entropy alloy: Comparison between experiment and calculation results, J. Alloys Compd. 719 (2017) 189–193, doi:10.1016/j.jallcom.2017.05.175.
[46] N.D. Stepanov, D.G. Shaysultanov, M.S. Ozerov, S.V. Zherebtsov, G.A. Salishchev, Second phase formation in the CoCrFeNiMn high entropy alloy after recrystallization annealing, Mater. Lett. 185 (2016) 1–4, doi:10.1016/j.matlet.2016.08.088.
[47] M.V. Klimova, D.G. Shaysultanov, S.V. Zherebtsov, N.D. Stepanov, Effect of second phase particles on mechanical properties and grain growth in a CoCrFeMnNi high entropy alloy, Mater. Sci. Eng. A. 748 (2019) 228–235, doi:10.1016/j.msea.2019.01.112.
[48] L. Li, Z. Li, A. Kwiatkowski da Silva, Z. Peng, H. Zhao, B. Gault, D. Raabe, Segregation-driven grain boundary spinodal decomposition as a pathway for phase nucleation in a high-entropy alloy, Acta Mater 178 (2019) 1–9, doi:10.1016/j.actamat.2019.07.052.
[49] C.-C. Hsieh, W. Wu, Overview of intermetallic sigma (σ) phase precipitation in stainless steels, ISRN Metall 2012 (2012) 732471, doi:10.5402/2012/732471.
[50] Y.H. Jo, W.M. Choi, D.G. Kim, A. Zargaran, K. Lee, H. Sung, S.S. Sohn, H.S. Kim, B.J. Lee, S. Lee, Utilization of brittle σ phase for strengthening and strain hardening in ductile VCrFeNi high-entropy alloy, Mater. Sci. Eng. A. 743 (2019) 665–674, doi:10.1016/j.msea.2018.11.136.
[51] H. Beladi, P. Cizek, P.D. Hodgson, Dynamic recrystallization of austenite in Ni-30 Pct Fe model alloy: microstructure and texture evolution, Metall. Mater. Trans. A 40 (2009) 1175–1189, doi:10.1007/s11661-009-9799-z.
[52] A.M. Wusatowska-Sarnek, H. Miura, T. Sakai, Nucleation and microtexture development under dynamic recrystallization of copper, Mater. Sci. Eng. A. 323 (2002) 177–186, doi:10.1016/S0921-5093(01)01336-3.
[53] T. Sakai, A. Belyakov, R. Kaibyshev, H. Miura, J.J. Jonas, Dynamic and post-dynamic recrystallization under hot, cold and severe plastic deformation conditions, Prog. Mater. Sci. 60 (2014) 130–207, doi:10.1016/j.pmatsci.2013.09.002.
[54] R. Gholizadeh, A. Shibata, N. Tsuji, Grain refinement mechanisms in BCC ferritic steel and FCC austenitic steel highly deformed under different temperatures and strain rates, Mater. Sci. Eng. A. 790 (2020) 139708, doi:10.1016/j.msea.2020.139708.
[55] R.R. Eleti, T. Bhattacharjee, L. Zhao, P.P. Bhattacharjee, N. Tsuji, Hot deformation behavior of CoCrFeMnNi FCC high entropy alloy, Mater. Chem. Phys. 210 (2018) 176–186, doi:10.1016/j.matchemphys.2017.06.062.
[56] N.D. Stepanov, D.G. Shaysultanov, N.Y. Yurchenko, S.V. Zherebtsov, A.N. Ladygin, G.A. Salishchev, M.A. Tikhonovsky, High temperature deformation behavior and dynamic recrystallization in CoCrFeNiMn high entropy alloy, Mater. Sci. Eng. A. 636 (2015) 188–195, doi:10.1016/j.msea.2015.03.097.
[57] A. Belyakov, T. Sakai, H. Miura, R. Kaibyshev, Grain refinement under multiple warm deformation in 304 type austenitic stainless steel, ISIJ Int 39 (1999) 592–599, doi:10.2355/isijinternational.39.592.
[58] N. Dudova, A. Belyakov, T. Sakai, R. Kaibyshev, Dynamic recrystallization mechanisms operating in a Ni-20%Cr alloy under hot-to-warm working, Acta Mater. 58 (2010) 3624–3632, doi:10.1016/j.actamat.2010.02.032.
[59] L. Blaz, T. Sakai, J.J. Jonas, Effect of initial grain size on dynamic recrystallization of copper, Met. Sci. 17 (1983) 609–616, doi:10.1179/030634583790420448.
[60] K.Y. Tsai, M.H. Tsai, J.W. Yeh, Sluggish diffusion in Co-Cr-Fe-Mn-Ni high-entropy alloys, Acta Mater. 61 (2013) 4887–4897, doi:10.1016/j.actamat.2013.04.058.
[61] D.B. Miracle, High-entropy alloys: a current evaluation of founding ideas and core effects and exploring “nonlinear alloys, JOM 69 (2017) 2130–2136, doi:10.1007/s11837-017-2527-z.
[62] A. Durand, L. Peng, G. Laplanche, J.R. Morris, E.P. George, G. Eggeler, Interdiffusion in Cr–Fe–Co–Ni medium-entropy alloys, Intermetallics 122 (2020) 106789, doi:10.1016/j.intermet.2020.106789.
[63] C. Zhang, F. Zhang, K. Jin, H. Bei, S. Chen, W. Cao, J. Zhu, D. Lv, Understanding of the elemental diffusion behavior in concentrated solid solution alloys, J. Phase Equilibria Diffus. 38 (2017) 434–444, doi:10.1007/s11669-017-0580-5.
[64] Z. Li, S. Zhao, S.M. Alotaibi, Y. Liu, B. Wang, M.A. Meyers, Adiabatic shear localization in the CrMnFeCoNi high-entropy alloy, Acta Mater 151 (2018) 424–431, doi:10.1016/j.actamat.2018.03.040.
[65] J. Joseph, N. Haghdadi, M. Annasamy, S. Kada, P.D. Hodgson, M.R. Barnett, D.M. Fabijanic, On the enhanced wear resistance of CoCrFeMnNi high entropy alloy at intermediate temperature, Scr. Mater. 186 (2020) 230–235, doi:10.1016/j.scriptamat.2020.05.053.